OSIRIS – THE SCIENTIFIC CAMERA SYSTEM ONBOARD ROSETTA

H. U. KELLER[1,*], C. BARBIERI[2], P. LAMY[3], H. RICKMAN[4], R. RODRIGO[5],
K.-P. WENZEL[6], H. SIERKS[1], M. F. A'HEARN[7], F. ANGRILLI[2], M. ANGULO[8],
M. E. BAILEY[9], P. BARTHOL[1], M. A. BARUCCI[10], J.-L. BERTAUX[11],
G. BIANCHINI[2], J.-L. BOIT[3], V. BROWN[5], J. A. BURNS[12], I. BÜTTNER[1],
J. M. CASTRO[5], G. CREMONESE[2,20], W. CURDT[1], V. DA DEPPO[2,22],
S. DEBEI[2], M. DE CECCO[2,23], K. DOHLEN[3], S. FORNASIER[2], M. FULLE[13],
D. GERMEROTT[1], F. GLIEM[14], G. P. GUIZZO[2,21], S. F. HVIID[1], W.-H. IP[15],
L. JORDA[3], D. KOSCHNY[6], J. R. KRAMM[1], E. KÜHRT[16], M. KÜPPERS[1],
L. M. LARA[5], A. LLEBARIA[3], A. LÓPEZ[8], A. LÓPEZ-JIMENEZ[5],
J. LÓPEZ-MORENO[5], R. MELLER[1], H. MICHALIK[14], M. D. MICHELENA[8],
R. MÜLLER[1], G. NALETTO[2], A. ORIGNÉ[3], G. PARZIANELLO[2], M. PERTILE[2],
C. QUINTANA[8], R. RAGAZZONI[2,20], P. RAMOUS[2], K.-U. REICHE[14], M. REINA[8],
J. RODRÍGUEZ[5], G. ROUSSET[3], L. SABAU[8], A. SANZ[17], J.-P. SIVAN[18],
K. STÖCKNER[14], J. TABERO[8], U. TELLJOHANN[6], N. THOMAS[19], V. TIMON[8],
G. TOMASCH[1], T. WITTROCK[14] and M. ZACCARIOTTO[2]

Abstract. The Optical, Spectroscopic, and Infrared Remote Imaging System OSIRIS is the scientific camera system onboard the Rosetta spacecraft (Figure 1). The advanced high performance imaging system will be pivotal for the success of the Rosetta mission. OSIRIS will detect

67P/Churyumov-Gerasimenko from a distance of more than 10^6 km, characterise the comet shape and volume, its rotational state and find a suitable landing spot for Philae, the Rosetta lander. OSIRIS will observe the nucleus, its activity and surroundings down to a scale of $\sim$2 cm px^{-1}. The observations will begin well before the onset of cometary activity and will extend over months until the comet reaches perihelion. During the rendezvous episode of the Rosetta mission, OSIRIS will provide key information about the nature of cometary nuclei and reveal the physics of cometary activity that leads to the gas and dust coma.

OSIRIS comprises a high resolution Narrow Angle Camera (NAC) unit and a Wide Angle Camera (WAC) unit accompanied by three electronics boxes. The NAC is designed to obtain high resolution images of the surface of comet 67P/Churyumov-Gerasimenko through 12 discrete filters over the wavelength range 250–1000 nm at an angular resolution of 18.6 μrad px^{-1}. The WAC is optimised to provide images of the near-nucleus environment in 14 discrete filters at an angular resolution of 101 μrad px^{-1}. The two units use identical shutter, filter wheel, front door, and detector systems. They are operated by a common Data Processing Unit. The OSIRIS instrument has a total mass of 35 kg and is provided by institutes from six European countries.

1. Introduction

1.1. History of the Instrument

On March 14th 1986 at 00:03 Universal Time, the European Space Agency's (ESA) spacecraft Giotto made its closest approach to comet 1P/Halley. The only remote sensing instrument onboard the spacecraft was the Halley Multicolour Camera (HMC), which was designed to image the nucleus and innermost coma of the comet from the spinning spacecraft. The instrument development was led by the Max-Planck-Institut für Aeronomie (now Max-Planck-Institut für Sonnensystemforschung, MPS) with the participation of several other major institutes in Europe (Keller *et al.*, 1995).

HMC was by far the most complex instrument onboard Giotto and a remarkable success (Figure 2). After the International Rosetta Mission (hereafter 'Rosetta') was selected as the 3rd Cornerstone Mission of ESA's Horizon 2000 programme, it was natural for a significant part of the HMC team to come together again to build the imaging system for the main spacecraft. Groups from MPS, the Laboratoire d'Astronomie Spatiale in Marseille (now Laboratoire d'Astrophysique de Marseille, LAM), the Osservatorio Astronomico di Padova (UPD), the Belgian Institute for Space Aeronomy (BISA), the Rutherford Appleton Laboratory (RAL) and the Deutsches Zentrum für Luft- und Raumfahrt (DLR) started working together in 1995 to study a modern imaging system that would be powerful enough to maintain Europe's lead in the remote sensing of cometary nuclei. The resulting proposal for the Optical, Spectroscopic, and Infrared Remote Imaging System OSIRIS was the only experiment proposed to ESA as the main imaging system on the Rosetta spacecraft in response to ESA's Announcement of Opportunity (AO).
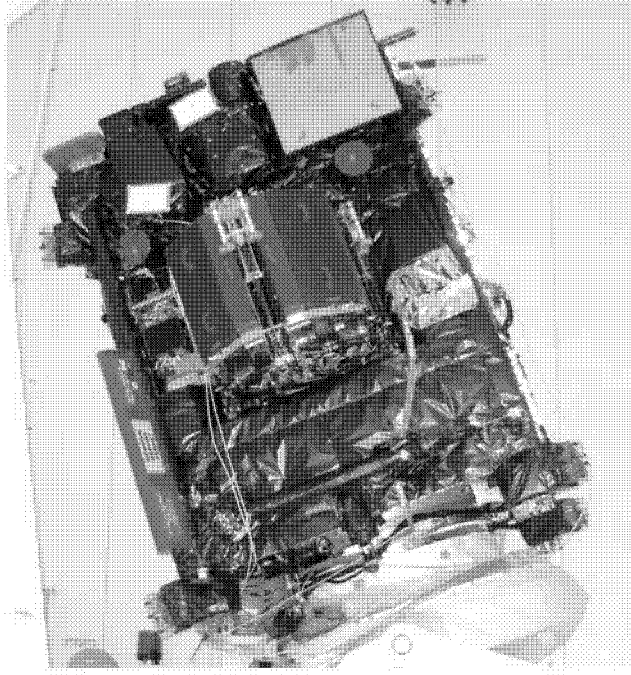
Figure 1. The two OSIRIS cameras units (*top left*, with white radiators) with VIRTIS and the Philae lander mounted on the −x panel of Rosetta.

The proposal included two cameras units (one narrow angle, one wide angle) with an infrared imager incorporated into the narrow angle system (Thomas *et al.*, 1998). There was also the possibility to include a UV spectrometer to cover the wavelength range from 200 to 400 nm. The instrument was extremely ambitious.

The Rosetta mission definition study, or 'Red Report', which outlined the goals and implementation of the mission, included a dedicated scientific imaging system as part of the strawman payload. However, funding problems led to considerable uncertainty as to whether the ESA Member States could fund such an ambitious imaging system. These problems were resolved about one year after the selection of the rest of the payload when a descoped version of OSIRIS was finally approved. The descoped version eliminated the IR imaging element of the cameras (the main interest of the Belgian and UK partners, BISA and RAL). However, additional support was offered by a group of Spanish laboratories led by the Instituto de Astrofísica de Andalucía (IAA), by ESA's Space Science Department (now Research and Scientific Support Department, RSSD) and by the Astronomical Observatory of Uppsala (now Department of Astronomy and Space Physics, DASP) in Sweden. The contributions from the different institutes finally involved in the OSIRIS instrument development are listed in Table I.

OSIRIS was delivered to ESA and integrated on the Rosetta spacecraft in 2002. The launch of Rosetta, originally foreseen for January 2003, was deferred
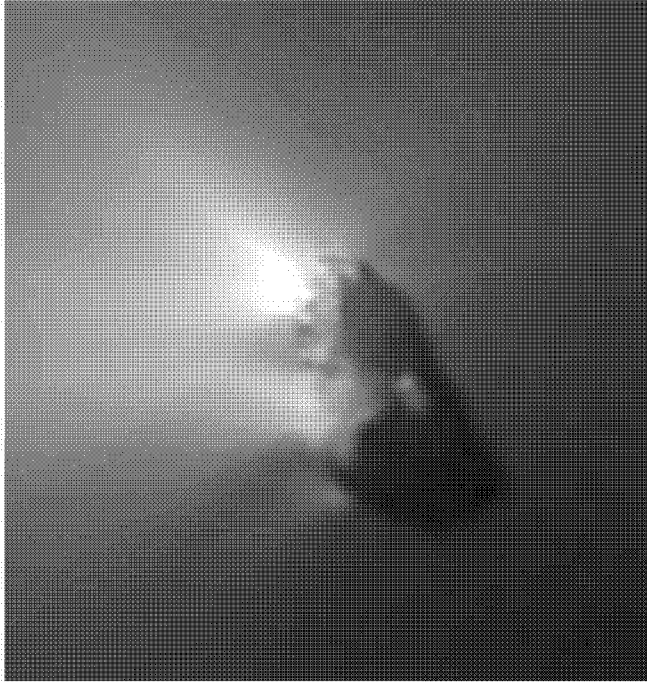
Figure 2. The nucleus of comet 1P/Halley as observed on March 14th, 1986, by the Halley Multi-colour Camera onboard the Giotto spacecraft.

to early 2004, changing the target comet from 46P/Wirtanen to 67P/Churyumov-Gerasimenko. OSIRIS was successfully commissioned in-flight during the months after the exciting launch on March 2nd 2004 and in the meantime has been used for scientific measurements of comet 9P/Tempel 1 in the course of the Deep Impact mission (Keller *et al.*, 2005; Küppers *et al.*, 2005).

1.2. THE OSIRIS NAME AND SYMBOL

The name, OSIRIS, standing for Optical, Spectroscopic, and Infrared Remote Imaging System, was selected at the time of the first instrument proposal, which included infrared imaging capability and the possibility of an ultraviolet spectrometer. Although several aspects of the original instrument were descoped, the name was retained.

Osiris was the Egyptian god of the underworld and of vegetation. He was the brother and husband of Isis who gave birth to their son, Horus, after his death. He was killed by the rival god, Seth. As legendary ruler of predynastic Egypt and god of the underworld, he symbolised the creative forces of nature and the indestructibility of life. The name was selected for the imaging system because Osiris is

TABLE I

Tasks of the OSIRIS consortium.

Task	Responsible institute
Overall responsibility and project management, system engineering, interfaces, Focal Plane Assemblies, CCDs and Readout Boards, HK Boards, integration & qualification of E-Boxes, harnesses, system integration, high-level software, NAC & WAC system calibration, QA, mission operations	MPS
NAC telescope, camera integration and qualification	LAM
WAC optical bench, camera integration and qualification, shutter mechanisms and shutter electronics, Front Door Mechanisms (mechanisms for NAC and WAC)	UPD
Mechanism Controller Board	IAA
Filter Wheel Mechanisms, E-Box Power Converter Module, NAC & WAC CRB Power Converter Modules	INTA
Data Processing Unit	RSSD
Mass memory, low-level software and data compression	IDA
NAC & WAC Filters	DASP
Thermal and structural analysis, NAC MLI, WAC FPA MLI	UPM

MPS – Max-Planck-Institut für Sonnensystemforschung (Germany), LAM – Laboratoire d'Astrophysique de Marseille (France), UPD – University of Padova (Italy), IAA – Instituto de Astrofísica de Andalucía (Spain), INTA – Instituto Nacional de Técnica Aeroespacia (Spain), RSSD – Research and Scientific Support Department (The Netherlands), IDA – Institut für Datentechnik und Kommunikationsnetze (Germany), – DASP Department of Astronomy and Space Physics (Sweden), UPM – Universidad Politécnica de Madrid (Spain).

identified with the 'all-seeing eye' that is depicted in the hieroglyph of his name (Figure 3).

1.3. FORTHCOMING SECTIONS

In Section 2, an overview of the key questions in cometary physics is presented. This is followed by a short section that describes the dual camera concept under which OSIRIS was developed. In Section 4, the detailed scientific rationale and objectives of the instrument are described. The subsequent sections describe the hardware in detail. We begin with the optical active elements (Sections 5–7), followed by the filter wheel mechanisms (Section 8), the shutter systems (Section 9) and the front door mechanism (Section 10). In Section 11 we deal with the image acquisition system. In Sections 12 to 16, we describe the overall control electronics, the digital interfaces, the onboard software, the EGSE and the telemetry. The calibration and operations are described in Sections 17 and 18. A conclusion completes the paper.
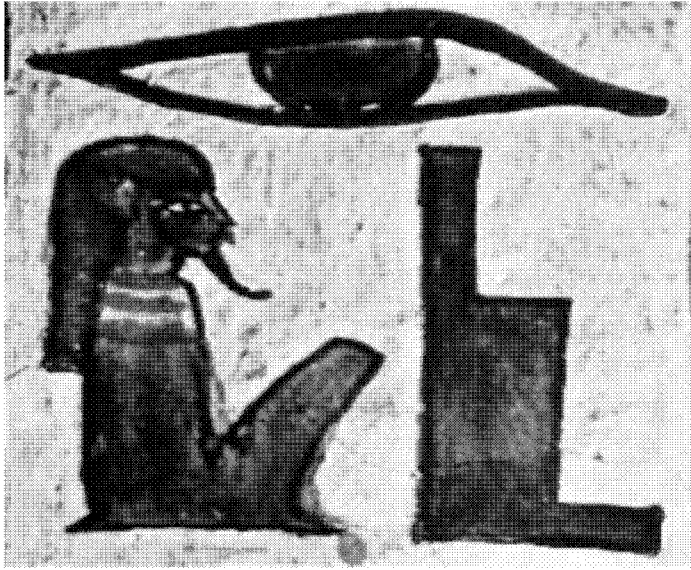
Figure 3. The hieroglyph of Osiris from the tomb of Nefertari, Thebes, nineteenth dynasty.

2. The Origin of Comets and Solar System Formation

Cometary missions such as Rosetta derive their greatest intellectual excitement from their potential to address questions about the origin of the Solar System. In order to apply data acquired by spacecraft missions to our understanding of these questions, it is necessary to understand in detail the physical and chemical processes that might occur in, on, and near the nucleus.

Some of the key problems of the cosmogony of comets and the Solar System include the nature of the accretion process in the protoplanetary disc, the physical and chemical conditions (temperature, pressure, molecular composition) that prevailed there, the relationship between the original interstellar composition (both gaseous and solid) and the disk composition, and the variation of its properties with both time and heliocentric distance. To derive the maximum scientific return, the camera system on Rosetta was designed to address as many of these questions as possible.

The size distribution of planetesimals and the degree to which they come from different parts of the protoplanetary disc can be studied directly by images from which the heterogeneity of a cometary nucleus at all scales can be determined. Images can show the chemical heterogeneity both on the surface and in the material released from the interior, the structural heterogeneity as seen in activity and in topography and its changes with erosion, and porosity and its variations as seen in the bulk density and moments of inertia. Heterogeneity at the largest scales, from comet to comet, is then studied by comparison of the results from Rosetta
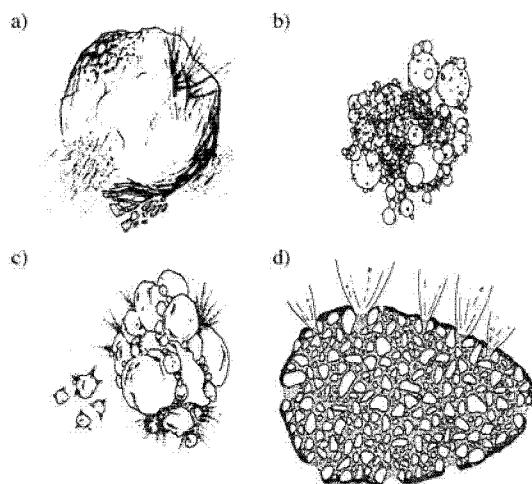
Figure 4. Conceptual models of the structure of the cometary nucleus: (a) Whipple's icy conglomerate, (b) fluffy aggregate, (c) primordial rubble pile, (d) icy-glue (Weissman, 1986; Donn, 1991).

with results for other comets (such as 1P/Halley, Borelly, Wild 2, and Tempel 1). This comparison will show whether or not phenomena such as resonances and instabilities in the protoplanetary disc are important in creating a characteristic size for planetesimals rather than a broad distribution of sizes characteristic of agglomeration and collisional phenomena. Our lack of knowledge of the structure of cometary nuclei is illustrated by the competing models shown in Figure 4. Note particularly the differences in the scales of the inhomogeneities. These models are further distinguished by the way in which the building blocks adhere to one another. This can be studied by determining the relationship between outgassing and structural inhomogeneities and by analysing the changes in topography and structure as the comet goes from a nearly inert state to a very active state. It can also be addressed both by measuring the degree of mixing between refractories and solids on the surface of the nucleus and by analysing the material released from the nucleus. Species could be mixed at the microscopic level, at macroscopic levels that are still small compared to the size of the nucleus, or at scales comparable to the size of the nucleus. We need to know the scale of mixing in a cometary nucleus as this can tell us, for example, whether large sub-nuclei with different histories were brought together in the nucleus.

The physical and chemical composition of the protoplanetary disc can be studied with calibrated images that provide abundances of species that are sensitive to those conditions (such as the OH/NH ratio and various mineralogical ratios). Questions of the nature of physical and chemical variations within the disc can be addressed by comparisons, both among the components of comet 67P/Churyumov-Gerasimenko nucleus and among comets formed in different parts of the disc (e.g. by comparing the properties of a Jupiter-family comet from the Kuiper belt, like

67P/Churyumov-Gerasimenko, with the properties of a Halley-family comet, like 1P/Halley itself, originally from the Uranus-Neptune region).

It is also necessary to understand the evolution of comets, since the changes that have occurred over a comet's active lifetime will have affected the observable properties of the nucleus. Do comets disappear by gradually shrinking in size as the ices sublime, do they disintegrate because of the activity, or do they become inert by choking off the sublimation? Are the intrinsic changes important compared to the extrinsic changes (collisions, perturbations that dramatically change the orbit, etc.)? How do comets contribute to the population of interplanetary dust, and how do they contribute to the population of near-Earth objects? The Rosetta mission and OSIRIS, in particular, are well suited to study the evolution over a large fraction of an orbit and to determine the actual contribution per orbital period to interplanetary dust. They are also well suited to study the evolution of the surface or mantle of the comet in order to address, for example, the question whether devolatilisation is more or less important than simple loss of the surface layers. Data obtained by Rosetta will be compared to those of missions to Near-Earth Asteroids.

Our understanding of the nature and origin of comets, and our use of them as probes of the early Solar System, is critically dependent upon understanding the cometary sublimation processes, because this knowledge is needed before we can relate results from Earth bound remote sensing to the nature of cometary nuclei. Although many processes in the outer coma, beyond about 100 km, are well understood already, the processes at the surface of the nucleus and in the near-nucleus portion of the coma, closer than a few cometary radii, are poorly understood and in some cases simply unknown. We need to understand the process by which material leaves the nucleus. Are observed variations in the 'dust-to-gas' ratio caused by intrinsic differences in the bulk ratio of refractories to ice, or are the variations dominated by properties and processes near the surface such as gas flow and structural strength? Does the size distribution of the particles change in the near-nucleus region because of either vaporisation or fragmentation or both? What fraction of the volatiles is released directly from the nucleus and what fraction is released subsequently from particles in the inner coma? Is the gas released from vaporisation at the surface or at some depth below the surface? Do periodic variations in the properties of the mantle occur and do they lead to variations in the coma that are, in fact, unrelated to the bulk properties of the nucleus?

OSIRIS will directly determine the outflow of gas and dust from different regions of the nucleus and will compare those variations with variations in surface mineralogy, in topography, and in local insolation. This will provide the context in which to interpret the results from the Rosetta lander (Philae). The unique strength of OSIRIS is the coverage of the whole nucleus and its immediate environment with excellent spatial and temporal resolution and spectral sensitivity across the whole reflected solar continuum up to the onset of thermal emission. In the next section, we briefly describe the imaging concept of OSIRIS. In the subsequent sections, we will address the many, detailed observational programmes to be

carried out by OSIRIS and how they bear on the fundamental questions outlined above.

3. NAC and WAC – a Complementary System

During the proposal phase, it was immediately obvious that the scientific objectives of the camera system on Rosetta would best be served by a combination of a Narrow Angle Camera (NAC) and a Wide Angle Camera (WAC). The NAC would be a system with high spatial resolution that would allow an initial detection of the nucleus, study its structure and rotation from relatively great distances (typically 10^4 km), investigate the mineralogy of the surface, and study the dust ejection processes. The WAC would have much lower spatial resolution but, accordingly, a much wider field of view. This would allow observations of the 3-dimensional flow-field of dust and gas near the nucleus and, in addition, would provide a synoptic view of the whole nucleus. In summary, the WAC would provide long-term monitoring of the entire nucleus from close distances, while the NAC would study the details. The two camera units have therefore been designed as a complementary pair, which, on the one hand, addresses the study of the nucleus surface, and on the other, investigates the dynamics of the sublimation process. The resulting cameras have the basic parameters shown in Table II.

Optical designs with central obscuration are notorious for their stray light problems. Therefore, off-axis designs with no central obscuration were selected for both

TABLE II

Basic parameters of the NAC and WAC units.

	NAC	WAC
Optical design	3-mirror off-axis	2-mirror off-axis
Detector type	$2k \times 2k$ CCD	$2k \times 2k$ CCD
Angular resolution (μrad px^{-1})	18.6	101
Focal length (mm)	717.4	140 (sag)/131 (tan)
Mass (kg)	13.2	9.48
Field of view ($°$)	2.20×2.22	11.35×12.11
F-number	8	5.6
Spatial scale from 1 km (cm px^{-1})	1.86	10.1
Typical filter bandpass (nm)	40	5
Wavelength range (nm)	250–1000	240–720
Number of filters	12	14
Estimated detection threshold (m_V)	21–22	18

systems. These provide maximum contrast between the nucleus and the dust. The internal baffle of the cameras was optimised for stray light suppression.

The NAC angular resolution was chosen as a compromise between requests for a high resolution required for investigation of unknown scale lengths on the nucleus surface, the need to maintain the nucleus in the FOV of the WAC when only a few nucleus radii above the surface, and the mass requirements for a longer focal length system. A spatial resolution of $\sim$2 cm px^{-1} was favoured, corresponding to an angular resolution of $\sim$20 μrad px^{-1} at a distance of 1 km. This value is also well adjusted to the limited data volume that can be transmitted back to Earth.

The NAC focal ratio (F-number) was set at 8, which is a compromise between speed (required at high heliocentric distance, r_h) and mass. Extensive calculations were performed to compute the motion of the image footprint over the surface during the mapping phase taking into account the orbit of the spacecraft and the rotation of the target, which would produce image smear. The calculations indicate that exposure times shorter than 50 ms are probably not required, given the resolution of the NAC. The WAC observations of the dust and gas environment require narrower filter bandwidths. Therefore the WAC exposure times are significantly longer.

The major considerations for the CCDs were:

- 'full well' signal-to-noise ratio (in order to optimise the dynamic range of the instrument)
- UV response (to give good signal-to-noise ratio for gas species)
- high Quantum Efficiency (QE) in the range 800 to 1000 nm (information on olivine and pyroxene bands).

A $2k \times 2k$ backside illuminated detector with a UV optimised anti-reflection coating was selected. This type of device has high QE over an extended wavelength range. Full-well dynamic range for these devices is of the order of 2×10^4. Over-exposure control is needed to allow saturation on the nucleus while acquiring high signal-to-noise information on the dust and gas. Custom CCDs with lateral anti-blooming were developed for OSIRIS. For cost reasons, identical devices are used in the two cameras.

While the two cameras have different scientific objectives, the similar nature of the instruments naturally led to our seeking cost reduction through development of identical subsystems. Hence, the mechanical design was adjusted so that identical Focal Plane Assemblies (FPA) could be used. The large format CCD necessitated the use of a mechanical shuttering of the exposure. Here again, identical subsystems were designed.

The requirement to determine the chemical and physical structure of the nucleus and the inner coma suggested the use of an extensive filter set. Identical filter wheels were used in the two cameras although each camera had its own filter complement adapted specifically for its own science goals.

Both cameras need protection from dust impacts when not operating. Hence, they have doors which can be opened and closed on command. Although the apertures
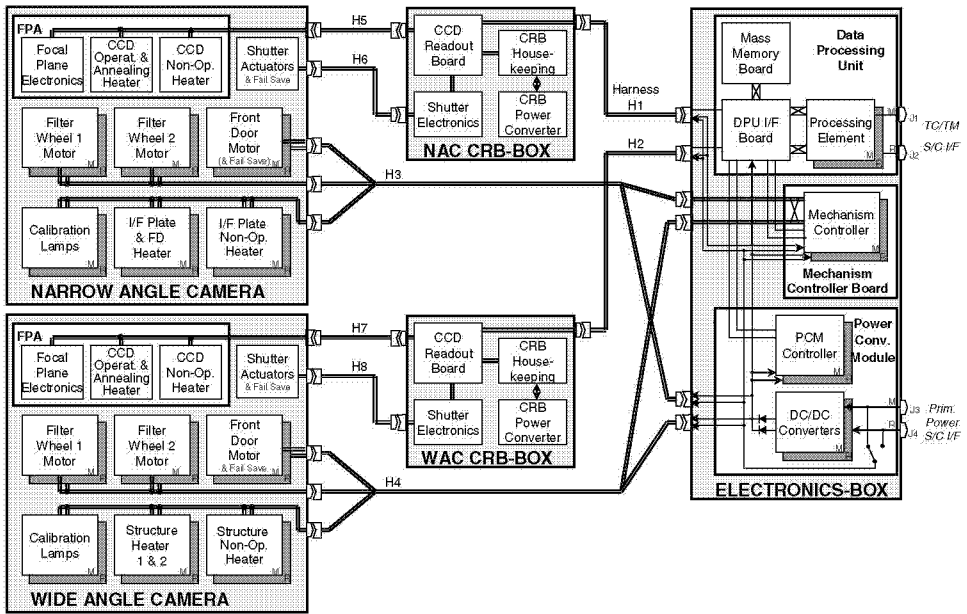
Figure 5. Block diagram of the OSIRIS functional blocks (M: main, R: redundant).

(and therefore the doors themselves) are different, the drive mechanism is the same in both cases. In addition, the doors can be used to reflect light from calibration lamps mounted inside the baffles. The lamps in the NAC and the WAC are identical. The modular concept of OSIRIS functional blocks, mechanisms, and electronics subsystems can be seen in Figure 5.

The selection of identical subsystems in both cameras reduced the management effort, cost, and overall complexity considerably, although interface definition and specification to accommodate these subsystems was more difficult throughout the project and required additional spacecraft resources (mass). The flight OSIRIS instrument consists of two camera units and 3 electronics boxes with related harnesses, a total of 22 subsystems, with a total mass of 35 kg and an average operational power consumption of 34 W.

4. Scientific Objectives

4.1. THE COMETARY NUCLEUS

The imaging systems on the Giotto, Vega, DS-1, Stardust, and Deep Impact spacecrafts were remarkably successful in providing our first glimpses of cometary nuclei and their immediate environments. Reviews of the results of these investigations can be found, e.g. in Keller *et al.* (1995, 2004), Tsou *et al.* (2004), and A'Hearn

et al. (2005). Despite this success, the imaging results were limited and many questions were left unanswered, and additional questions arose, many of which will be addressed by OSIRIS. We describe here the goals of our nucleus observations.

4.1.1. *Position and Size of the Nucleus*

The first goal of OSIRIS will be to localise the cometary nucleus and to estimate its size and shape as quickly as possible for mission planning purposes. These properties must be coarsely known well before the mapping phase commences. This determination should be performed near the end of the approach phase when the spacecraft is between 10^3 and 10^4 km from the nucleus. Determination of the radius to an accuracy of 10% from 10^4 km can be performed with the NAC and will immediately yield an estimate of the nucleus volume (and mass for an assumed density) accurate to about a factor of 2.

4.1.2. *Rotational State*

Another goal of OSIRIS is to determine the rotational properties of the comet including the periods of rotation about three principal axes, the total angular momentum vector L, the changing total spin vector and the characteristics of any precessional behaviour. Measurements of these quantities will constrain the range of possible inhomogeneities of the nucleus and will also permit the development of time-dependent templates over which other data sets may be laid. The secondary, more ambitious goal is to use OSIRIS to monitor the rotational properties throughout the entire mission to search for secular evolution in response to the torques acting on the nucleus caused by the onset of jet activity as the comet approaches perihelion. Model calculations indicate that for a small nucleus, such as 67P/Churyumov-Gerasimenko, torques could force re-analysis of the rotational properties of the nucleus on timescales of days (Gutiérrez *et al.*, 2005). The measured precession rate, along with an estimate of the average reaction force (from the non-gravitational acceleration of the nucleus) and an estimate of the torque caused by outgassing, may allow an estimate of the absolute value of the nucleus moment of inertia. This, in turn, would give clues to the internal density distribution, especially when combined with the gravity field determination (see Pätzold *et al.*, this volume), allowing us to distinguish between a lumpy, a smoothly varying, and a homogeneous nucleus (see also Kofman *et al.*, this volume). The structural inhomogeneity would provide an important clue for the size distribution of the forming planetesimals.

4.1.3. *Shape, Volume, and Density*

The concept of comets as uniformly shrinking spherical ice balls was shattered by the Giotto results. The nucleus is expected to be highly irregular on all scales as a consequence of cratering, outgassing, and non-uniform sublimation (Keller *et al.*, 1988). However, it is not clear whether these irregular-shaped bodies reflect

the shape of the nuclei at their formation, or are the result of splitting during their evolution, or are caused by non-uniform sublimation.

To accurately model such a craggy shape, techniques developed at Cornell University (Simonelli *et al.*, 1993) can be used. Although OSIRIS has no stereo capability *per se*, the motion of Rosetta relative to the nucleus can be used to produce stereo pairs. The shape model will be based upon these stereogrammetric measurements in addition to limb and terminator observations. Once the shape model is available, it can be used to determine the surface gravity field and moments of inertia and will also be used to reproject and mosaic digital images, as well as to develop surface maps. This technique has yielded accurate shapes for the Martian moons and Galileo's asteroid targets, 951 Gaspra and 243 Ida (Thomas *et al.*, 1995, 1994).

To look for internal inhomogeneities of say 30% implies that differences in the geometrical and dynamical moments of inertia need to be known to better than 10%. We therefore need to measure both to better than 1%. Thus, the topography must be characterised over the entire nucleus to an accuracy of ± 20 m.

4.1.4. *Nucleus Formation and Surface Topography*

On the smallest scales, the building blocks comprising the cometary nucleus may be a heterogeneous mixture of interstellar and interplanetary dusts and ices, with a structure and composition reflecting the physical conditions and chemistry of the protoplanetary disc. The different accretion processes leading to the production of first, grains, then, building blocks and, finally, cometary nuclei, are all expected to have left their mark on a nucleus which has remained largely unaltered since its formation. OSIRIS will therefore perform a detailed investigation of the entire cometary surface over a range of spatial scales as wide as possible to identify the hierarchy of cometary building blocks.

In addition to its implications for nucleus formation, the topography of the surface determines the heat flow in the uppermost layers of the nucleus (Gutiérrez *et al.*, 2000; Colwell, 1997). High resolution imaging will determine the normal to the surface and hence provide input to surface heat flow calculations.

The Vega 2 TVS observations of jets were interpreted as showing a fan generated from a few, kilometre-long, quasi-linear cracks (Smith *et al.*, 1986; Sagdeev *et al.*, 1987). If fresh cracks appear on the surface during the aphelion passage, then OSIRIS will be able to probe the inner layers of the nucleus where some stratification is expected from the loss of volatiles near the surface.

4.1.5. *Colour, Mineralogy, and Inhomogeneity*

Inhomogeneity of mineral composition and colour could provide the most obvious clues to the size of building blocks. The Vega and Giotto cameras were able to determine only rough estimates of the broad-band ($\lambda/\Delta\lambda = 5$) colour of the nucleus of 1P/Halley. OSIRIS will allow a much more sophisticated study of the mineralogy

of the nucleus surface by recording images that span the entire wavelength range from 250 to 1000 nm.

OSIRIS also has the opportunity to search for specific absorption bands associated with possible mineral constituents. The wavelengths of pyroxene absorptions are highly dependent upon their exact structure (Adams, 1974). Hence, filters giving complete coverage of the 750 nm to 1 μm regions at 60 nm resolution were incorporated. Vilas (1994) suggested that the 3.0 μm water of hydration absorption feature of many low albedo (including C-class) asteroids strongly correlates with the 700 nm $Fe^{2+} \rightarrow Fe^{3+}$ oxidised iron absorption feature. Given the spectral similarity between C-class asteroids and 1P/Halley and the high water ice content in comets, a search for the water of hydration feature at 700 nm will be made.

4.1.6. *Surface Photometry*

Due to the limited information from high-velocity fly-bys, little was learned of the photometric properties of the surface of comet 1P/Halley. The correct determination of the phase function for comet 67P/Churyumov-Gerasimenko will provide information on the surface roughness through application of, for example, Hapke's scattering laws (Hapke, 1993). The Philae observations will provide the parameters necessary to validate the surface roughness models used to interpret global data provided by OSIRIS.

4.1.7. *Polarization Measurements*

The properties that can be addressed by polarization measurements can be obtained more accurately by observations of the surface from the Philae or by *in situ* analysis. Implementation of polarization measurements in OSIRIS was thought costly in terms of resources and calibration, and they were therefore not included.

4.1.8. *Active and Inactive Regions*

Modelling (Kührt and Keller, 1994) suggests that debris from active regions will not choke the gas and dust production in view of the highly variable terrain, the extremely low gravity, and the lack of bonding between particles forming the debris. Inactive regions can only arise if either the material comprising the regions formed in the absence of volatiles or, alternatively, if the regions have become depleted in volatiles without disrupting the surface.

To verify this picture, a comparison of active and inactive regions on comet 67P/Churyumov-Gerasimenko must be of high priority. If inactive regions are merely volatile-depleted with respect to active regions, high signal-to-noise observations at several wavelengths may be required to differentiate between the two. Imaging of the interface between active and inactive regions may provide evidence of surface structures and tensile strength present in one type of region, but not in the other.

As the observations of 'filaments' indicate (Thomas and Keller, 1987), there is no reason to suppose that active regions are homogeneous. Activity may be

restricted within an active region (see for example the theoretical calculations of Keller *et al.*, 1994). For this reason, OSIRIS will identify the active fraction within what we call an active region. Achieving this goal may lead to understanding how cometary activity ceases, leaving an inert comet. Do inactive spots within active regions spread to reduce cometary activity or does the infall of material from the edge of the sublimation crater choke emission?

Directions of jets and locations of active spots are influenced by topography. The distribution and orientation of near-nucleus jets can be used to infer topographic features (Thomas *et al.*, 1988; Huebner *et al.*, 1988). OSIRIS will investigate these correlations.

4.1.9. *Physics of the Sublimation Process*
The physical processes characterising the sublimation and erosion processes in or above active regions depend on the physical structure of the surface and the distribution of refractory and volatile material within the nucleus. Dust particles have usually been treated as impurities in the ice (icy conglomerate). Starting with the interpretation of the images of 1P/Halley (Keller, 1989), it has become clear that the topography requires a matrix dominated by refractory material (Küppers *et al.*, 2005). The other extreme is the model of a friable sponge, where the refractory material is intimately mixed with the ice and where the erosion process maintains a balance between the ice and dust. How are dust particles lifted off the surface? The excellent resolution of the OSIRIS NAC, which will be smaller than the mean free path of the gas near the surface, will allow the detection and study of the relevant macrophysical processes.

4.1.10. *The Diurnal Cycle*
OSIRIS will be able to monitor short-term changes in active regions very easily. Changes are most likely when active regions cross the terminators. Cooling will lead to decreased activity, but on what timescale? On the other hand, as the insolation increases, will there be changes in the surface structure?

4.1.11. *Outbursts*
Outbursts (or rapid increases in the brightness of cometary comae) have frequently been observed from the ground and recently also during the approach of the Deep Impact spacecraft to comet 9P/Tempel 1. This implies some sudden increase or even explosion of activity ripping the surface crust apart. OSIRIS, and in particular the WAC, can be used to monitor autonomously the nucleus activity over many months at various scales. The NAC can then be used to look in detail at the source to determine how the site has altered topographically and spectrally.

4.1.12. *Mass Loss Rate*
The floor of the active regions will be lower by several metres on average after the passage of comet 67P/Churyumov-Gerasimenko through its perihelion. It is clear

that if an active area can be monitored by OSIRIS at a resolution of ≈30 cm the mass loss will be evident. If the density of the surface layer can be determined by Philae or through joint OSIRIS/Radio Science investigations, this is potentially the most accurate means to determine the total mass loss rate particularly if the mass loss is dominated by infrequently emitted large particles.

4.1.13. *Characterisation of the Landing Site*
The NAC was designed to remain in focus down to 1 km above the nucleus surface. Mapping at ~2 cm px^{-1} will reveal inhomogeneities of the nucleus at scale lengths comparable to the size of Philae. Homogeneous sites would provide no difficulties in interpretation but heterogeneous sites may be scientifically more interesting. As a result, OSIRIS needs to be able to characterise the landing site and to identify on what types of terrain Philae has landed.

4.1.14. *Observation of the Philae Touchdown*
There is no guarantee that the orbiter will be able to observe Philae when it strikes the surface. However, OSIRIS will provide valuable information on the impact velocity, the result of the initial impact, and the final resting position and orientation.

Outgassing from the impacted site may also occur. If fresh ice is so close to the surface that the lander can penetrate the crust, emission of gas and dust may be fairly vigorous. If so, OSIRIS can quantify this emission with highest possible spatial and temporal resolution.

4.2. NEAR-NUCLEUS DUST

The near-nucleus dust environment of a comet is remarkably complex and remains poorly understood. Understanding the near-nucleus environment is necessary to understanding the nucleus itself. OSIRIS can investigate global dust dynamics.

4.2.1. *Detection of Emission at Rendezvous*
OSIRIS will be used to place constraints on distant activity of the nucleus. It is evident, however, that detection of dust in the vicinity of the nucleus will be extremely difficult at high heliocentric distances. The dust production may decrease as steeply as $r_h^{-2.9}$ (Schleicher *et al.*, 1998), with a corresponding decrease in flux proportional to $r_h^{-4.9}$. At 3.25 AU, we estimate the ratio of the signal received from the dust to that from the surface $(I_d/I_s) \approx 4 \times 10^{-4}$ based on scaling of Giotto measurements. Therefore, to quantify the total dust production rate, a dynamic range of >2000 is required. Both the WAC and the NAC were designed with this contrast requirement.

4.2.2. *Temporal Evolution*
4.2.2.1. *Variation with Heliocentric Distance.* HMC observations showed that the dust production rate of comet 1P/Halley during the Giotto fly-by was remarkably

stable over the three hours of the encounter. Ground-based observations have shown, however, that comets exhibit large and rapid changes in dust production. A key goal of OSIRIS will be therefore to monitor the variation in the production rate and to compare it to the rotational characteristics of the nucleus and the change in r_h.

4.2.2.2. Variations with Rotation. The lack of significant variation in the dust production rate with the rotation seen at comet 1P/Halley was not expected. How does the production vary with the solar zenith angle? How long does an active region take to switch on after sunrise? These phenomena are determined by the physical properties (*e.g.* the thermal conductivity) of the surface layer. If sublimation occurs below the surface then a period of warming may be required before dust emission starts. The surface layer could act as a buffer to stabilise the activity. These questions can be addressed using OSIRIS to monitor the active region during the first minutes after it comes into sunlight.

4.2.2.3. Night Side Activity and Thermal Inertia. The inferred absence of night side activity during the Giotto fly-by and the thermal map created from near-infrared spectral scans of comet 9P/Tempel 1 during the recent Deep Impact mission (A'Hearn *et al.*, 2005) suggest that the thermal inertia must be low. Observations of comet Hale–Bopp (C/1995 O1) also suggest that the thermal inertia of comets is low (Kührt, 2002). The high porosity of the surface and the resulting low thermal conductivity suggest that the activity should decrease rapidly and stop when the energy source is removed. Monitoring the dust emission as an active region crosses the evening terminator can confirm this hypothesis.

4.2.2.4. Short-Term Variability. The dust emission from the nucleus of comet 1P/Halley showed no evidence for short-term (order of minutes) temporal varia-tions. Because of the nature of the active regions one might expect, however, that the emission should occasionally show an enhanced or reduced rate on a timescale of perhaps a few seconds. A sudden burst offers the possibility of following the emitted dust and using it to derive streamlines and velocities in the flow. This obser-vation would provide strong constraints on the hydrodynamics of the flow and lead to increased understanding of the dust-gas interaction a few metres above active regions. If large enough, outbursts could also modify the flow field itself allowing us to use OSIRIS to monitor the reaction of the inner coma to changes in the emission rate.

4.2.3. *Large Particles in Bound Orbits*
It was shown that gravitationally-bound orbits around cometary nuclei are possible, in theory, for relatively small particles even in the presence of radiation pressure (Richter and Keller, 1995). In addition, evidence from radar measurements suggests that large clouds of centimetre-sized objects accompany comets in their orbits (Campbell *et al.*, 1989). The high resolving power of OSIRIS combined with our

proximity to the nucleus will allow us to place constraints on the number density of objects with a particle radius of $a > 5$ mm. Since it is now widely believed that most of the mass lost by comets is in the form of large particles (McDonnell *et al.*, 1991), observations of this phenomenon could prove very important in determining the dust to gas ratio. Clearly, it would be a major discovery to find an extremely large chunk which might be termed 'a satellite' of the nucleus. Active chunks, as seen in comet Hyakutake (Rodionov *et al.*, 1998), may also be evident.

4.2.4. *How Inactive are 'Inactive' Regions?*
The observations by HMC and more recent fly-bys (A'Hearn *et al.*, 2005) were not good enough to place firm constraints on the activity of so-called inactive regions. Dust emission from the illuminated but apparently inactive regions could have been up to 10% of the emission from active regions and remained undetected. This clearly has implications for the evolution of the nucleus and for the flow field of gas and dust emission about the nucleus.

4.2.5. *Optical Properties of the Dust*
The orbit of Rosetta and the broad-band filters in OSIRIS will allow observations of dust at many phase angles ($0°-135°$) over a wide wavelength range. The phase curve and colour are sensitive to particle size, composition, and roughness. Deduction of these properties and their variation with r_h will be important for ground-based observations of other comets since it will provide the single scattering albedo, the phase function, and the characteristic particle size.

4.2.6. *Eclipses*
Eclipse measurements are extremely interesting for the innermost dust coma as they would allow OSIRIS to determine the forward scattering peak of the dust phase function, which provides the best information on the size distribution and nature of the dust particles. The strong forward scattering peak also yields the most sensitive measurement of the dust column density (e.g. Divine *et al.*, 1986).

4.2.7. *Acceleration and Fragmentation*
Complications with the determination of local dust production rates arise if the observations cover the dust acceleration region, if fragmentation is significant, or if optical depth effects become important. Measurements of the acceleration will quantify the drag coefficient of the gas-particle interaction and characterise the near-surface Knudsen layer. The fulffiness of the cometary dust can be derived from these observations.

A complementary approach is to measure the radius and velocity of large escaping dust agglomerates in dependence of heliocentric distance. By knowing the gravitational forces, this would also provide information on the physics of the gas-dust interaction (drag coefficient) at and near the surface (Knudsen layer), on the cohesive forces, and on the density of the agglomerates.

4.3. GAS EMISSIONS

Our current understanding of the composition of the nucleus and variations within the nucleus is severely limited by our lack of knowledge about the processes in the innermost coma. We know little about the variations of the composition of the outgassing on any scale, although there are indications from Earth-based measurements of large-scale heterogeneity (e.g. in 2P/Encke and in 1P/Halley). There are distributed sources in the coma which produce some of the species in the coma, including H_2CO, CO, and CN. Because we cannot separate completely the extended coma source from the nuclear source, we cannot determine reliably the amount of ice in the nucleus. We therefore plan to make observations of the gas in order to address some of the most crucial questions in relating abundances in the coma to abundances in the nucleus.

4.3.1. *Selected Species*
In order to constrain the heterogeneity of other parent molecules, we will map the release of certain daughter species in the vicinity of the nucleus. Dissociation products having short lifetimes and identifiable parents are ideal for this task. In particular, NH at 336.5 nm and NH_2 at 570 nm will be measured to trace the heterogeneity of NH_3 (and thus the nitrogen chemistry in the nucleus), CS at 257 nm to trace the heterogeneity of CS_2 (and thus the sulphur chemistry), and OH at 309 nm and OI at 630 nm to trace H_2O.

   The heterogeneity of other fragments, such as CN (388 nm), will also be measured, even though we do not know the identity of the parent molecules, because these species show evidence of an extended source. The recent interest in the distribution of Na has led us to introduce a sodium filter at 589 nm.

4.3.2. *Sublimation Process and Inactive Areas*
The results from 1P/Halley showed us that the release of dust is confined to discrete active areas, comprising only a small fraction of the surface (15%). We have no information, however, on whether the gas is similarly confined. One of the key questions to be answered is whether gas is also released from the apparently inactive areas. The mapping capability of OSIRIS is ideally suited to answer this question and thereby to assess the effects of an inert layer on the release of gas and dust.

4.4. SERENDIPITOUS OBSERVATIONS

4.4.1. *Asteroid Fly-bys*
The fly-bys of 2867 Steins and 21 Lutetia will provide interesting secondary targets on the way to the comet. The main scientific goals of OSIRIS observations of the asteroids are:

   • Determination of physical parameters (size, volume, shape, pole orientation, rotation period)

- Determination of surface morphology (crater abundance, crater size distribution, presence of features such as ridges, grooves, faults, boulders, search for the presence of regolith)
- Determination of mineralogical composition (heterogeneity of the surface, identification of local chemical zones, superficial texture)
- Search for possible gravitationally bound companions (detection of binary systems).

4.4.2. *Mars Fly-by*

High-resolution images of Mars (>200 px across the planet) can be taken within two days of closest approach (cf. recent HST images). This will provide data on the global meteorological conditions on Mars and allow us to follow weather patterns over a period of about two days. Images around 12 h before closest approach would be of sufficient resolution to allow us to resolve vertical structures in the atmosphere at the limb and to estimate the global atmospheric dust content. The solar occultation during Mars fly-by would allow detection of the putative Martian dust rings.

4.4.3. *Earth-Moon System Fly-bys*

As with the space missions Galileo and Cassini/Huygens, the Rosetta remote sensing instruments can perform testing and calibration during the fly-bys of the Earth-Moon system. There are also several interesting possibilities for new science. For example, the Moon is now known to have a tenuous sodium atmosphere ('exosphere'). The Na filter on the WAC can be used to acquire maps of Na near the Moon. Similarly, OI emission from the Earth may be detectable at high altitudes. Vertical profiles of OI in the atmosphere of the Earth can be derived by stellar occultations.

5. The NAC Telescope

The Narrow Angle Camera is designed to obtain high-resolution images of the comet at distances from more than 500,000 km down to 1 km, and of the asteroids 2867 Steins and 21 Lutetia during the interplanetary cruise. The cometary nucleus is a low-albedo, low-contrast object; hence, good optical transmission and contrast-transfer characteristics are required. The camera also should be able to detect small ejected particles close to the comet nucleus (brightness ratio $\geq 1/1000$), placing strict tolerances upon stray light rejection.

The scientific requirements for the NAC translate into the following optical requirements. A square field of view (FOV) of width $2.2°$ and an instantaneous field of view (IFOV) of 18.6 μrad (3.8 arcsec) per pixel, a spectral range from 250 nm to 1 μm, and a moderately fast system (f/8) are needed. An unobstructed pupil is required to minimise stray light. This is particularly important for the study of gas and dust surrounding the bright nucleus. The requirements are fulfilled with

an all-reflecting system of 717 mm focal length and an off-axis field, using a 2048 × 2048 px, UV-enhanced CCD array. The high resolution over a large flat field requires a system of three optical surfaces.

5.1. OPTICAL CONCEPT AND DESIGN

A flat-field, three-mirror anastigmat system, TMA, is adopted for the NAC. Anastigmatism (freedom from third-order spherical aberration, coma, and astigmatism) is attained by appropriate aspheric shaping of the three mirror surfaces, and a flat field (zero Petzval sum) is achieved by appropriately constraining the system geometry. Our solution (Dohlen *et al.*, 1996) has an axial pupil physically placed at the second mirror M2, an off-axis field of view, appropriate baffle performance and a large back-focal clearance. The optics requires only two aspheric mirrors, the tertiary remaining spherical. This considerably reduces fabrication cost and alignment difficulty. The three mirror surfaces are rotationally symmetric about a common optical axis, but the field of view is sufficiently removed from the axis to ensure that all rays pass through the system without vignetting. Figure 6 shows a ray tracing diagram of the optical system. The mirrors are made of Silicon Carbide (SiC); details of their fabrication, polishing and alignment can be found in Calvel *et al.* (1999).

The system is equipped with two filter wheels placed in front of the CCD. In order to cope with the presence of ghost images (see Section 7.2.3), the filters are
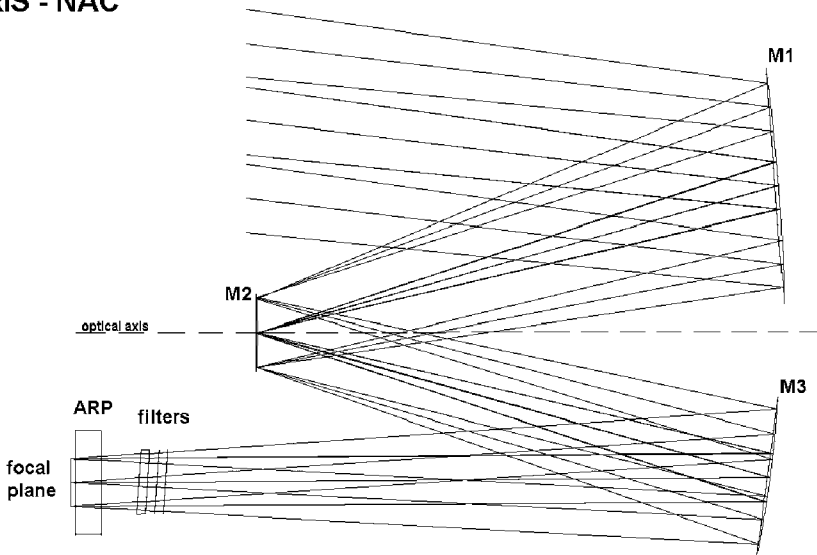

Figure 6. Ray paths through the NAC optical system.

tilted by $4°$ to the optical axis and wedged by $10'$. In addition to the bandpass filters, the filter wheels contain anti-reflection-coated focusing plates (Far Focus Plate FFP and Near Focus Plate NFP, see Table V), which, when used with the filters of the other wheel, allow two different focusing ranges: far focus (infinity to $2\,km$, optimised at $4\,km$) and near focus ($2\,km$ to $1\,km$, optimised at $1.3\,km$). Nominal operation is defined as far focus imaging with an orange filter (centered at 645 nm with a bandwidth of 94 nm). This filter has similar characteristics to that of the orange filter in the Halley Multicolour Camera.

A plane-parallel, anti-reflection coated plate, referred to as Anti-Radiation Plate (ARP), was added to the front of the CCD for radiation shielding. Its effect for monochromatic light is negligible, but the shift of focus is considerable for the two UV filters (Far-UV and Near-UV), and the Far-UV and focusing plates are affected by longitudinal chromatic aberration. Table III lists the construction parameters for the optimised camera design, including filter, focusing plate and ARP. The system includes an external baffle for stray light rejection and a front door for protection.

5.2. OPTICAL PERFORMANCE

Figure 7 shows spot diagrams and root-mean-square wave front errors (WFE) at six points in the FOV located at the centre, the edges and the corners. Since the system is symmetrical about the $y–z$ plane (see footnote in Table III), the characteristics are identical for positive and negative x co-ordinates. The wave front error is calculated for the central wavelength of the orange filter ($\lambda = 0.645\ \mu m$). As seen in Figure 7, the WFE is in the order of $0.04\ \lambda$ over the entire FOV. The performance is limited primarily by a triangular-type (trifle) aberration which is present in varying degrees over the entire FOV. Astigmatism and coma are close to zero at the centre but become significant towards the edges.

5.3. STRAY LIGHT REJECTION

The observation of faint cometary physical and chemical phenomena, such as dust and gas jets from localised vents on the nucleus, require good optical transmission and high contrast with strict tolerances on stray light. There are two types of stray light sources. One originates from the cometary nucleus itself (considered as an extended object), the image of which is in the focal plane. The second source is the sun, which is allowed to reach an elongation of $45°$ from the optical axis of the instrument.

Rejection of stray light from the nucleus is insured by the TMA design whose unobstructed pupil minimises diffraction phenomena and scattered light. A low level of micro roughness of the optical surfaces ($<2\,nm$ rms) was specified to limit the stray light contribution. The internal baffle of the instrument was optimised

TABLE III

Optical specifications for the NAC TMA; Far Focus Plate in wheel 1, Orange filter in wheel 2.

Component	Radius (mm)	Separation along z axis[a] (mm)	Conic constant or glass type	Diameter or $x \times y (\times z)$[a] (mm)	Centre y coordinate (mm)	Tilt of normal wrt. M2 axis (deg)
Entrance pupil	Flat	−690.0		89.4		−6.962
Primary	−1103.162	−304.0	CC = −1.65727	136	85.2[b]	0
Secondary	− 400.598	301.5	CC = −1.000	44.0	0	0
Tertiary	−626.583	−354.5	CC = 0.000	92	−82.9[b]	0
Filter 1, surface 1	Flat	−4.942[c]	Fused silica n (645 nm) = 1.4567	40 × 40 (× 5.000)	−86.00	−3.8333
Filter 1, surface 2	Flat	−5.00[c]				−4
Filter 2, surface 1	Flat	−4.687[c]	OG550 n (645 nm) = 1.5368	40 × 40 (× 4.746)		−4
Filter 2, surface 2	Flat	−25.724				−4.1667
ARP, surface 1	Flat	−12	Fused silica n (645 nm) = 1.4567	51.0	−86.15	0
ARP, surface 2	Flat	−8.056				0
CCD	Flat			27.7 × 27.7	−86.32	0

[a]z is along the M2 axis, y is in the plane containing z and the central object point, x is perpendicular to z and y.
[b]Geometrical centre of the mirrors. Impact of 'central' ray is slightly offset (∼0.5 mm).
[c]Distance along an axis tilted −4° to z-axis, perpendicular to filter wheel plane.

(0°, 1.1°)
$WFE_{rms} = 0.040\,\lambda$

(1.1°, 1.1°)
$WFE_{rms} = 0.039\,\lambda$

(0°, 0°)
$WFE_{rms} = 0.032\,\lambda$

(1.1°, 0°)
$WFE_{rms} = 0.031\,\lambda$

(0°, -1.1°)
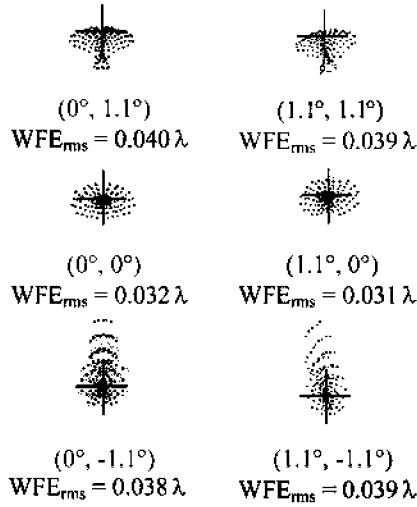$WFE_{rms} = 0.038\,\lambda$

(1.1°, -1.1°)
$WFE_{rms} = 0.039\,\lambda$

Figure 7. Spot diagrams for six positions in the NAC FOV. The cross is 5 μm wide. RMS wavefront errors are given for the centre wavelength of the Orange filter.

by adding vanes and protective black tapes in critical areas. An internal black foil envelops the whole instrument to prevent light leakage.

Rejection of stray light from the sun requires an external baffle, which can be closed with the front door whenever the solar elongation is less than 45°. The fraction of the power incident onto the detector surface to that entering the aperture of the telescope baffle was required to be $< 10^{-9}$ at angular distances from the centre of the FOV exceeding 45°. The external baffle comprises a two stage cylinder with four vanes, which have a square aperture with rounded corners to fit around the scientific beam. The baffle is made of aluminium alloy and all internal surfaces are coated with a black paint. The vanes have a thickness of 0.5 mm with sharpened edges in order to reduce the reflecting area.

5.4. NAC STRUCTURE

The main function of the structure of the NAC is to carry the three mirrors of the TMA, the dual filter wheel mechanism, shutter mechanism, focal plane assembly, the external baffle, the front door mechanism (Figure 8), and to maintain them in proper position during the long interplanetary cruise and the phases of nucleus observations.

The basic concept is an athermal design, achieved by using the same material for the mirrors and the supporting structure. Therefore the optical properties are maintained during temperature changes, as long as thermal gradients are limited. Silicon carbide, a very rigid ceramic material with good thermal
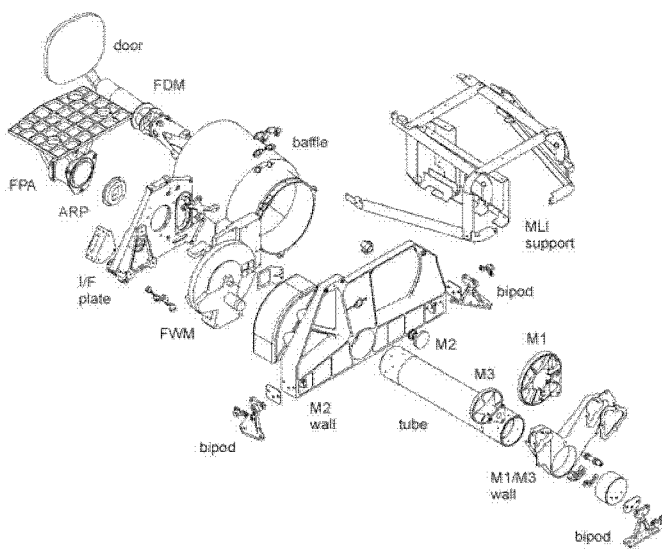
Figure 8. The NAC assembly (see also Figure 9). Focal plane and front door are on the *upper left*, primary and tertiary mirrors on the *lower right*.

properties (low coefficient of thermal expansion, good thermal conductivity), is used.

The structure is U-shaped with two walls cemented on a connecting tube, see Figure 9. The main wall carries the external baffle, the secondary mirror and a magnesium interface plate (I/F plate), which receives the mechanisms and the focal plane. The second wall carries the primary and the tertiary mirrors, which are bolted directly on it. The thickness of the two walls is reduced to the minimum feasible in order to minimise mass. The NAC structure is kinematically mounted on the main spacecraft structure via three titanium bipods, decoupling it from panel distortion and reducing thermal flows.

5.5. THERMAL DESIGN

The athermal concept requires that thermal gradients be minimised. A thermal decoupling is necessary between the SiC parts constituting the telescope and the subsystems, which have to be maintained within their temperature ranges. The I/F plate is connected to the main SiC wall via three flexible titanium blades and insulator washers. The entrance baffle and the Front Door Mechanism (FDM) are connected to the main SiC wall via three insulator washers. In order to minimise thermal losses, the instrument is wrapped in a thermal blanket made of Multi-Layer Insulation (MLI). The strong limitation on available power during the cruise phase required a careful optimization of the thermal design. With a
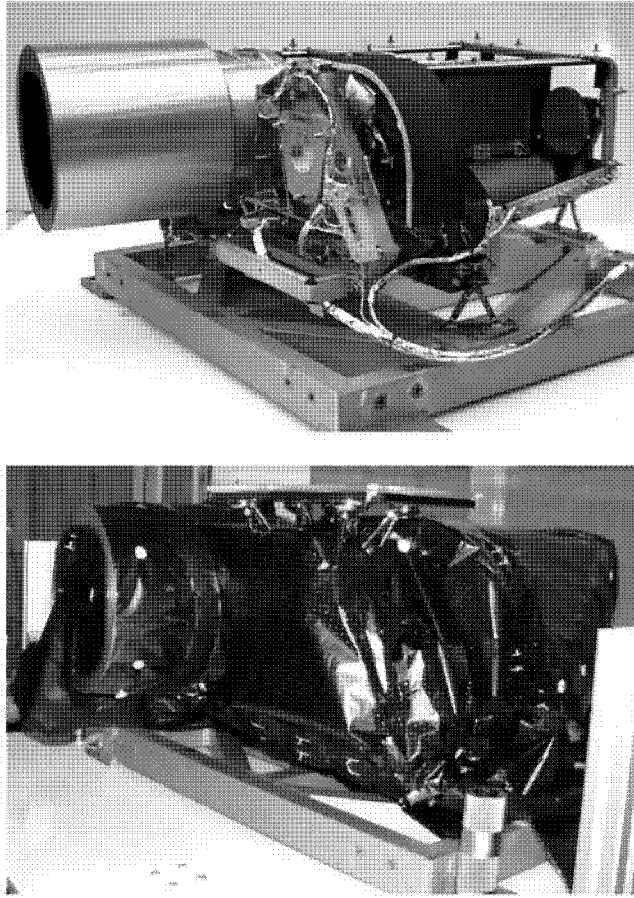
Figure 9. NAC Flight Model during integration and in flight configuration.

non-operational power of 7.5 W, the subsystems are maintained in their allowed temperature ranges, while the SiC telescope can float to a minimum temperature of $-70\,^\circ$C.

5.6. INTERNAL CALIBRATION

The internal calibration of the NAC is achieved by illuminating the rear side of the lid of the front door, which acts as a diffusing screen. The illumination system is composed of two redundant sets of two small lamps placed inside the external baffle, between two vanes. The four lamps form a rectangle but only two lamps on one side are lit at a time. The colour temperature of the tungsten lamps is 2,410 K; they have a quartz envelope and are mechanically mounted with a glass diffuser. The in-flight calibration system provides a reference illumination to the camera

in cruise for comparison to the ground calibration flat fields. Deviations allow the determination of long-term degradation in flight.

6. The WAC Telescope

The prime objective of the Wide Angle Camera is the study of the weak gas and dust features near the bright nucleus of the comet. For this purpose, the WAC has to satisfy a number of scientific requirements. The WAC needs a rather large field of view, $12° \times 12°$, to observe both the nucleus and the features of emitted gas and dust. It has to cover a relatively wide spectral range, from UV to visible, and it has to provide a high contrast ratio, of the order of 10^{-4}, to be able to observe the bright nucleus and the weak coma simultaneously.

6.1. OPTICAL CONCEPT AND DESIGN

To obtain the required camera performance, an unobstructed all-reflective, off-axis optical configuration using two aspherical mirrors was adopted. With this system, best performance over the entire field of view is obtained, providing a spatial resolution of about 20 arcsec. The all-reflective solution, unlike a lens design, allows observation in the ultraviolet spectral range. The unobstructed solution provides the optimal contrast ratio. With the $20°$ off-axis design, the whole field of view can be covered without significant aberrations. Moreover, a fast $f/5.6$ ratio was adopted to allow detection of the cometary nucleus and of the asteroids from a distance of 10^6 km in 1 s exposure time. The characteristics of the optical solution are summarised in Table IV.

6.2. TWO-MIRROR OFF-AXIS SYSTEM

The concept of the WAC optical design is shown in Figure 10; it is described in more detailed in Naletto *et al.* (2002). The primary mirror (M1) collects the light from the object at an angle of $20°$ with respect to the camera axis and reflects it towards the secondary mirror (M2), which focuses the light onto the focal plane assembly. In contrast to the majority of all-reflective cameras, in which the instrument stop is located on the primary mirror, the WAC stop coincides with M2. Figure 11 shows the flight mirrors prior to their assembly. To assure a good reflectivity over the whole spectral range, the mirrors were aluminized and protected with MgF_2.

The instrument design includes a set of 14 wedged filters. The filters are mounted on two wheels. The filter set comprises narrow and wide bandpasses for observations of emission bands and lines, and of the continuum. A 4 mm thick Suprasil Anti-Radiation Plate (ARP) was installed directly above the CCD.

TABLE IV

Characteristics of the WAC design.

| Optical concept	All reflective, two-mirror 20° off-axis design, unobstructed, unvignetted; axis of off-axis: y
FOV	11.35° (y) × 12.11° (x)
Encircled energy	>80% inside a pixel of 13.5 μm sq.
FL at centre of FOV	Tangential: 131 mm, sagittal: 140 mm
Average image scale at the centre of FOV	7.4 mrad mm^{-1} equiv. 101 μrad px^{-1}
Distortion of the field	Barrel type
FL in x	128.0–133.4 mm
FL in y	139.2–140.0 mm
Residual geometric distortion	<2.5% along the tangential direction <1% along the sagittal direction
Refocusing	No refocusing necessary for distance range 500 m to infinity
Nominal F-number	$F/5.6$
Wavelength range	240–720 nm
Overall reflectivity	52% at $\lambda = 245$ nm to 88% at $\lambda = 500$ nm
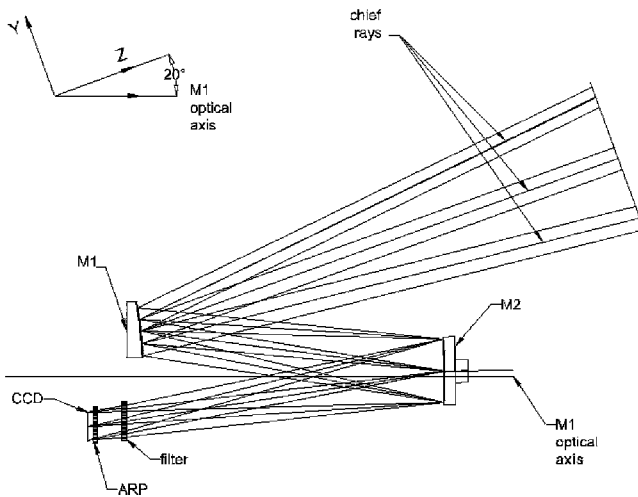
Figure 10. WAC optical concept with the two mirrors, the filter and the anti-radiation plate in front of the CCD detector.

The sun angle is greatly variable when in orbit around the comet nucleus. To protect the system from direct sun light, a movable front door is positioned at the instrument entrance aperture. Moreover, to reduce the stray light into the instrument, a rather complex baffle system was realised (Debei *et al.*, 2001; Brunello *et al.*, 2000).
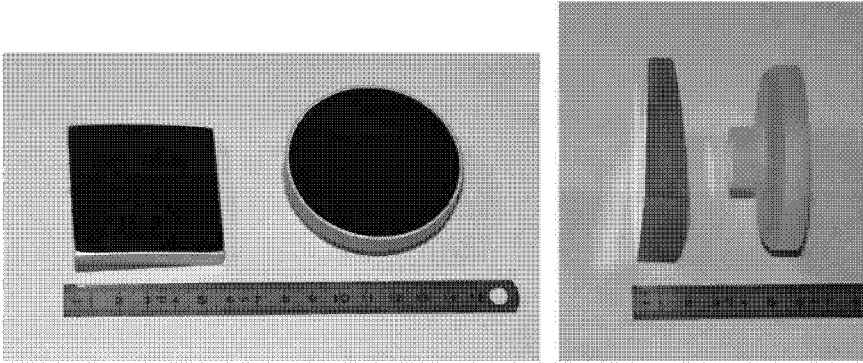
Figure 11. WAC mirror blanks M1 (*left*) and M2 (*right*).

6.3. OPTICAL PERFORMANCE

Figure 12 shows the spot diagrams at the centre, the edges, and the corners of the FOV. The square boxes correspond to the pixel size. The geometrical performance of the camera is optimised with residual aberrations essentially lower than the pixel size. The diffraction effect is negligible, with more than 90% of the energy falling into a single pixel. The optical performance is maintained essentially unchanged from infinity down to almost 500 m, so that no refocusing system is required.
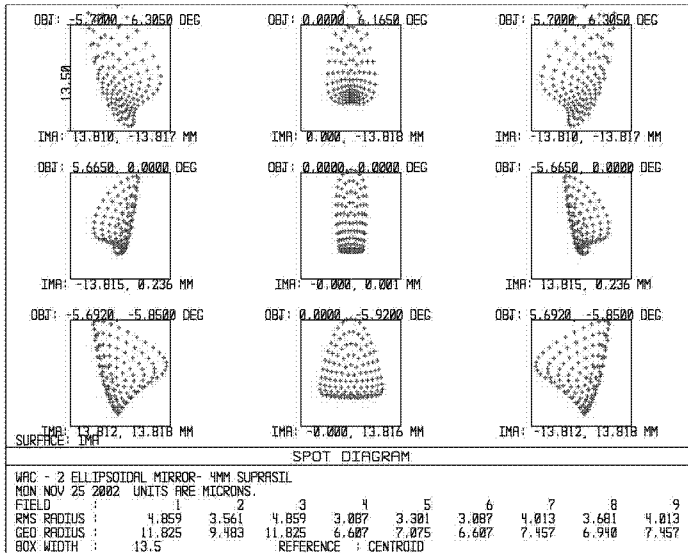

Figure 12. WAC spot diagram. The spots refer to the centre, the edges and the corners of the 12° × 12° FOV. The boxes correspond to the pixel size of the detector.

The off-axis design produces slightly different scales in the image plane: the scale in y is almost constant, $19.9\,\mathrm{arcsec\,px^{-1}}$, while the scale in x direction varies from $20.9\,\mathrm{arcsec\,px^{-1}}$ to $21.8\,\mathrm{arcsec\,px^{-1}}$. The acquired field width seen by the CCD is subsequently about $11.35°$ in y and between $12.09°$ and $12.16°$ in x direction (coordinate system see Figure 10).

The nominal photometric aperture, that is the projection of the M2 stop onto the primary mirror, is circular with a radius of 12.5 mm. However, the distortion causes the aperture to be slightly elliptical and position dependent. The corresponding photometric distortion can be removed during calibration of the images.

6.4. STRUCTURE OF THE CAMERA

The lightweight, stiff structure is based on a closed box made of aluminium alloy machined by electro-erosion. The optical bench ribs are optimised to prevent noise induced through vibration and to minimise vibration amplification at interfaces with mechanisms. For thermo-structural stabilization, three kinematic mounting feet and an external baffle are implemented. A truss structure was designed to improve the thermal decoupling between the external baffle and the optical bench, and to minimise the temperature gradient. The telescope is covered by a thermal blanket, while the inner parts were painted with electrically conductive black paint. The optic supports are made of the same material as the optical bench to minimise distortion.

6.5. THERMAL BEHAVIOUR

The WAC thermal control system was designed for the operational temperature range of the optical bench, $12 \pm 5°\mathrm{C}$. This requirement is derived from the tolerances in the position of the telescope optical elements.

The total electrical power dissipated into the camera is less than 2 W. The heat leak of the Focal Plane Assembly (FPA) is in the order of 1 W. With only 1 W to dissipate, the camera should be thermally insulated from the environment. Thus, the whole external surface was covered with MLI and the WAC was mounted to the spacecraft with insulating feet made of a titanium alloy (Figure 13). The strongest disturbance to the WAC thermal control is due to the large optical aperture, an area of about $300\,\mathrm{cm^2}$, which can point towards many different thermal sources.

The external baffle is the most critical element of the WAC thermal design. A trade-off analysis was performed. A glass reinforced epoxy structure with absorber coating, thermally insulated from the camera, was shown to be the best solution. To extend the operational capability for sun incidence angles below $45°$, a radiator was added to the upper part of the baffle to reduce the heat flux to the camera. Below $45°$, operation of the WAC is intermittent, with observational phases until the allowed upper temperature limit is reached, followed by phases of cooling with closed door.
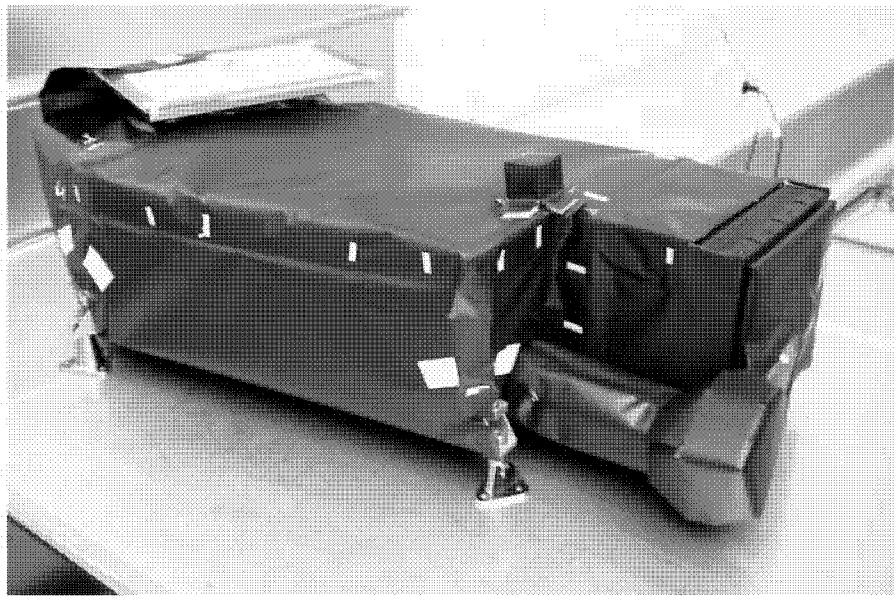
The other important requirement for the camera thermal control system is to provide a temperature greater than $-40\,^{\circ}$C during the non-operative phases. This is achieved using a heater dissipating 5 W.

6.6. Baffle System and Stray Light Performance

The primary scientific requirement for the WAC is to be able to image dust and gas in the proximity of the comet nucleus at heliocentric distances from 3.25 AU to perihelion. The WAC baffle system has therefore to perform two different functions: First, to attenuate light from any source, e.g. the sun at angles larger than $45°$, to at least 4×10^{-9} (at the detector). The second function is related to the characteristic of the WAC optical design with the system stop located at the second mirror M2. Light entering the system aperture and reaching M1, not being collected by M2, acts as internal source of stray light. The baffle has to attenuate this stray light contribution by a factor of at least 10^{-3}.

The baffle system is made of two main parts: the first (external baffle) with rectangular cross section is localised in front of the M1 mirror and has 17 vanes, the second (internal baffle) is accommodated between M2 and the detector, and has 4 deep vanes (see Figure 14).

6.7. Calibration Lamps

The calibration lamps used in the WAC are identical to the NAC lamps. They are flame-formed bulb lamps with a colour temperature of 2410 K. Four lamps (two
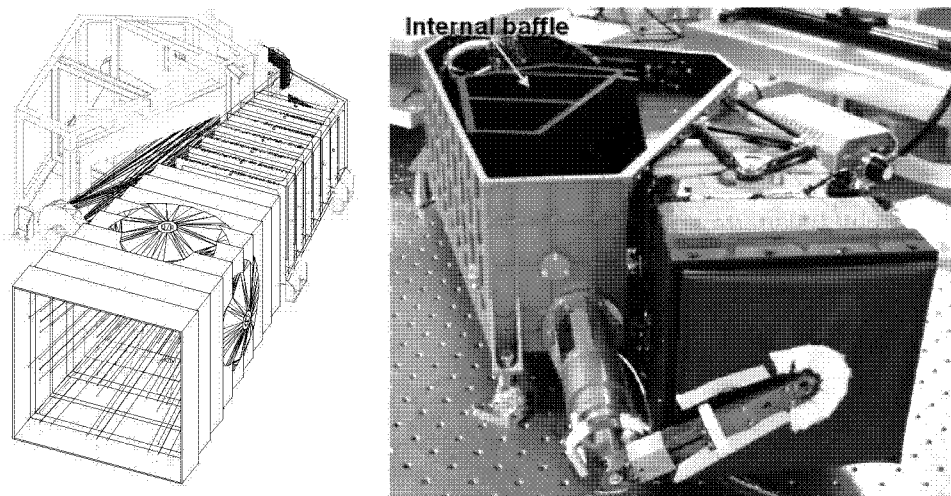
Figure 14. Concept and view of the WAC baffle.

main and two redundant) are mounted at the fifth vane of the external baffle. The lamps illuminate the inside of the front door, which diffuses the light into the optical path. Obviously, this illumination cannot provide a flat field, but a reference illumination pattern monitoring the system transmission.

7. Interference Filters

Sets of 12 filters for the NAC, and 14 for the WAC, were selected. The NAC filters will be used to characterise the reflectivity spectrum of the nucleus surface over as wide a spectral range as possible, and to focus in particular on some possible or likely absorption bands. With no need for isolating narrow spectral features, the bandpasses are generally wider than for the WAC, i.e. typically from 24 to 100 nm.

For the WAC, the principal aim is to study the intensity of gas emissions and dust-scattered sunlight as functions of position and viewing angle in the vicinity of the nucleus. This is accomplished by centring narrow bandpass filters on a set of emission lines with slightly broader bandpass filters to measure the continuum.

7.1. SELECTED FILTERS

7.1.1. *NAC Bandpass Filters*
The 12 selected filters for the NAC are shown in Table V. The NAC filters were optimised to provide a low resolution spectrum from 250 nm to 1 μm. The orange filter at 650 nm will allow a close comparison of the results from comet

TABLE V

Filters of the narrow angle camera.

Name	Wavelength (nm)	Bandwidth (nm)	Peak Trans. (%)	Objective	Thickness at centre (mm)	Wheel
FFP-UV	250–850		>99	UV focusing plate for use of filters in wheel 2	4.41	1
FFP-Vis	250–1000		>95	Vis focusing plate for use of filters in wheel 2	5.00	1
FFP-IR	300–1000		>99	IR focusing plate for use of filters in wheel 1	5.15	2
NFP-Vis	300–1000		>98	Vis focusing plate for near-nucleus imaging	4.18	1
Far-UV	269.3	53.6	37.8	Surface spectral reflectance	4.50	2
Near-UV	360.0	51.1	78.2	Surface spectral reflectance	4.68	2
Blue	480.7	74.9	74.6	Surface spectral reflectance	4.67	2
Green	535.7	62.4	75.8	Surface spectral reflectance	4.64	2
Neutral	640.0	520.0	5.0	Neutral density filter	4.64	1
Orange	649.2	84.5	92.4	surface spectral reflectance HMC orange filter	4.73	2
Hydra	701.2	22.1	87.4	Water of hydration band	4.72	2
Red	743.7	64.1	96.0	Surface spectral reflectance	4.68	2
Ortho	805.3	40.5	69.8	Orthopyroxene	4.69	1
Near-IR	882.1	65.9	78.4	Surface spectral reflectance	4.75	1
Fe_2O_3	931.9	34.9	81.6	Iron-bearing minerals	4.73	1
IR	989.3	38.2	78.1	IR Surface reflectance	4.74	1

67P/Churyumov-Gerasimenko with those obtained from comet 1P/Halley with HMC. A cluster of filters was placed in the wavelength range between 800 nm and 1 μm to investigate possible pyroxene and olivine absorptions. A neutral density filter was added to reduce the photon flux from the comet in the event that very bright, pure ice structures are revealed by activity near perihelion. The neutral density filter can also be used if the shutter fails and will be used for resolved observations of the Earth and Mars.

Clear filter substrates with anti-reflection coating (cf. near and far focusing plates) were included to modify the focus position by adjustment of the optical thickness so that the NAC remains in focus down to a distance of just 1 km from the target. The thickness of each bandpass filter was chosen individually (dependent upon wavelength and substrate refractive index) to maintain the system in focus.

7.1.2. *WAC Bandpass Filters*

The 14 selected filters for the WAC are shown in Table VI. Most of the filters are narrow band filters to study gas and radical emissions. The minimum filter bandwidth allowed by the *f*/5.6 optical design is 4 nm, because narrower bandpass filters would produce variations in the transmitted wavelength over the field. Continuum filters were incorporated to allow straightforward subtraction of the dust continuum from images acquired in gas emission filters. Calculations indicate that high signal-to-noise ratios in CN, OH, OI, and CS will be easily achieved. Na, NH, and NH_2 should be detectable in binned data within 1.2 AU from the Sun. A broad-band R filter was included for nucleus detection and mapping, in the event of failure of the NAC. A green filter, identical to that in the NAC, was included for simple cross-correlation of the data between NAC and WAC. No refocusing capability is required for the WAC.

7.2. ORIENTATION AND PROPERTIES

7.2.1. *Materials and Radiation Tolerance*

Radiation tests were performed to ensure that the performance of the filters is not seriously degraded by cosmic ray damage during the 9 years in cruise. Many of the substrates are made of Suprasil, which is known to be radiation hard, but some filters are Schott coloured glasses to achieve a proper out-of-band blocking. Since too little was known about the radiation hardness of such glasses, and unacceptable damage levels could not be excluded, laboratory experiments with the Uppsala tandem Van de Graaff accelerator were performed. A 2 MeV proton beam was shot onto OG590, KG3, and Suprasil blanks to simulate the solar proton exposure during the Rosetta cruise. The resulting change in spectral transmission was measured (Possnert *et al.*, 1999; also Naletto *et al.*, 2003).

Figure 15 illustrates the obtained results by Possnert *et al.* (1999). The total proton fluence of 10^{13} cm^{-2} exceeds the expected fluence for Rosetta by almost two orders of magnitude. Other experiments using smaller fluences or lower dose

TABLE VI

Filters of the Wide Angle Camera.

Name	Wavelength (nm)	Bandwidth (nm)	Peak Trans. (%)	Objective	Thickness at centre (mm)	Wheel
Empty				Empty position to allow the use of filter wheel 2		1
Empty				Empty position to allow the use of filter wheel 1		2
UV245	246.2	14.1	31.8	Continuum surface spectral reflectance	4.51	1
CS	259.0	5.6	29.8	CS gas emission	4.60	1
UV295	295.9	10.9	30.4	Continuum for OH	4.75	1
OH-WAC	309.7	4.1	26.0	OH emission from the vicinity of the nucleus	4.82	1
UV325	325.8	10.7	31.6	Continuum for OH surface spectral reflectance	4.85	1
NH	335.9	4.1	23.6	NH gas emission	4.86	1
UV375	375.6	9.8	57.3	Continuum for CN surface spectral reflectance	4.60	2
CN	388.4	5.2	37.4	CN gas emission	4.61	2
Green	537.2	63.2	76.8	Dust continuum cross-correlation with NAC	4.71	1
NH_2	572.1	11.5	60.9	NH_2 gas emission	4.74	2
Na	590.7	4.7	59.0	Sodium gas emission	4.75	2
VIS610	612.6	9.8	83.4	Continuum for OI surface spectral reflectance	4.65	2
OI	631.6	4.0	52.4	O (^{1}D) gas emission for dissociation of H_2O	4.66	2
R	629.8	156.8	95.7	Broadband filter for nucleus and asteroid detection (NAC redundancy)	4.67	2

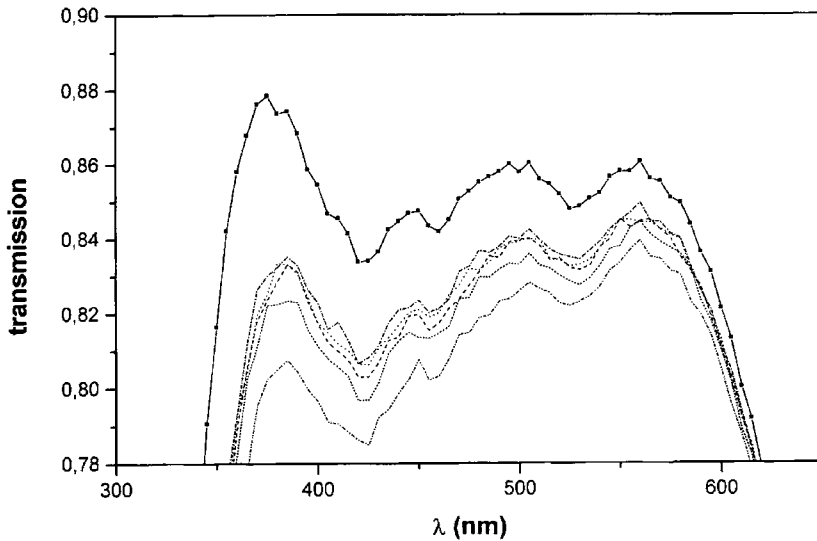*Figure 15.* Transmission curves for KG3 glass. The bold curve provides the transmission prior to irradiation to a proton fluence of 10^{13} cm^{-2}. The dashed curves show the recovery of transmission with time at room temperature.

rates yielded much smaller effects, and the general conclusion is that the expected damage levels are indeed acceptable. Moreover, the figure shows that annealing at room temperature causes a rapid recovery towards the initial transmission. The experiments on Suprasil verified that no visible damage occurred in this case.

7.2.2. *Physical Parameters*
The filters are placed relatively close to the detector in the optical path. This minimises the size of the filters but, because of the large CCDs used by OSIRIS, the required aperture is still fairly large. The required clear aperture is 37.5×37.5 mm^2. The physical size of the applied filters is therefore 40.0×40.0 mm^2 with rounded corners. They are wedged to reduce ghosts and are optimised for operation at $+10°$C.

7.2.3. *NAC Ghosts*
The NAC suffers from a complex combination of ghost images due to three transmission elements in front of the CCD: the filters, the focusing plate and the Anti-Radiation Plate (ARP). Two types of ghosts may be distinguished. The 'narcissic' ghosts are caused by light reflected from the CCD surface and back reflected from transmissive elements. Filter ghosts are caused by two successive reflections from transmissive elements.

The ghost images are out-of-focus replicas of the scientific image, and the amount of defocus is different for each ghost image according to the extra optical path travelled. For a point source, the diameter of the ghost image increases with

increasing optical path, and so the ghost intensity decreases. For extended objects however, such as the comet nucleus, the integrated ghost intensity is independent of defocus distance and equals the product of the two reflections encountered.

In order to take advantage of cases where one ghost type is weaker than the other, the two types are physically separated. This is achieved by introducing a $4°$ tilt of the filter wheel, hence of filters and focusing plates, with respect to the optical axis, sending filter ghosts to one side of the scientific beam and narcissic ghosts to the other side. The slight dispersion effect introduced by this tilt is compensated by the $10'$ wedge of the filters. Also, ghost reflections from the focusing plates are reduced by using specialised plates for the UV, visible and IR ranges.

The most problematic ghost components are produced by the ARP and the CCD. While efforts were made to reduce their reflectance over the entire wavelength range, ghost performance is optimised in the orange/red region, where other performance criteria (stray light rejection, efficiency, etc.) are also optimal. In this region, ghost intensity of less than 10^{-3} is required.

7.2.4. *WAC Narcissic Ghosts*

The peculiar orientation of the WAC filters with respect to the light beam has to be emphasised. The beam incidence is not normal. The non-wedged surface of the filter is parallel to the CCD plane which is orthogonal to the camera optical axis. The angle between the optical axis and the central ray of the light beam depends on filter thickness and wheel position, e.g. $8.75°$ for the green filter in filter wheel 1 and $8.9°$ for the red filter in filter wheel 2. The thickest filter side is towards the filter wheel rotation axis.

The thicknesses of the WAC filters were calculated to have the same focus shift for all filters taking into account the focus shift introduced by the Anti-Radiation Plate (ARP).

Ghost minimization with suitable anti-reflection (AR) coatings for the WAC is even more stringent than for the NAC because of the initial contrast requirements. Analysis of the ghost images has shown that the secondary narcissic ghost is the most intense one. This ghost is produced by back-reflection of the beam from the CCD surface and the outermost filter surface. The ratio of total narcissic ghost over image intensity depends on the actual filter and is between 0.16 (worst case, for NH filter) and 10^{-3} (best case, for Green and R filters).

8. Filter Wheel Assembly

The Filter Wheel Mechanism, FWM, positions the optical filters in front of the CCD detectors with high accuracy. The assembly is composed of

- a support structure
- a common shaft with two parallel filter wheels
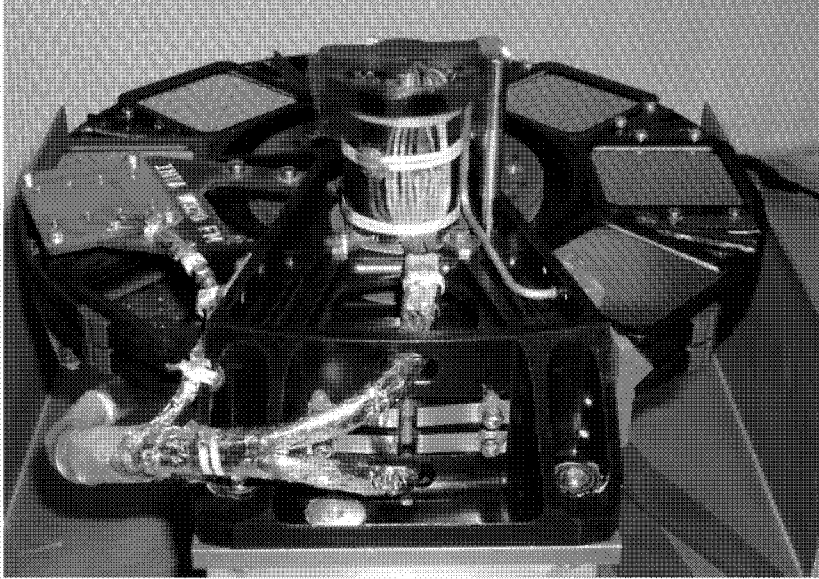
Figure 16. Filter Wheel Mechanism. Two *V*-shaped flat springs lock the filters by the Vespel cams. Reed switches are activated by encoder magnets to identify the filter in front of the CCD.

- two stepper motors with gears (crown and pinion)
- position encoders and mechanical locking devices.

Figure 16 shows the fully assembled FWM. The mechanism provides the space for 16 optical elements (12 filters and 4 focusing plates in the NAC, 14 filters and an empty position per wheel in the WAC). The selected filters for both cameras are described in Section 7.1.

Each filter wheel is turned by a stepper motor to position a filter in front of the CCD in less than 1 s (half wheel turn). All filters are positioned with an accuracy of ± 135 μm (10 CCD pixels) relative to the optical axis with ± 30 μm of repeatability (two pixels). The positioning accuracy is achieved by V-shaped Vespel cams, one on top of each filter, which are locked by stationary V-shaped stainless steel springs attached to the mechanism support.

8.1. FILTER ACCOMMODATION

Each wheel has eight square openings to accommodate the filters. The filters are mounted in cover frames of aluminium alloy and further positioned by elastic joints, which preclude damage to the filter's surface upon thermal expansion. In order to minimise light reflection, all mechanism surfaces (except the gear teeth, the pinion and the motor fixation) are finished in black.

8.2. WHEEL DRIVE MECHANISM

Due to the tight mass, power and timing allocations, titanium alloy was selected for the central shaft, while aluminium alloy is used for the filter wheels and for the assembly support. The filter wheel support has three mechanical interface points to the camera that allow adjustment by shimming to obtain the required alignment to the optical path.

The wheels are mounted to the central shaft by double ball bearings, coupled back-to-back with 50 N pre-load. These space-qualified bearings are dry-lubricated by lead ion sputtering of the stainless steel races. The wheels support the Vespel crown gear at one side. The pinion on the motor shaft is made of stainless steel. The gap between the pinion and the crown is adjusted to 50 μm, which is equivalent to 0.07° backlash in the wheel. SAGEM 11PP92 type stepper motors were fabricated with redundant windings and were further modified to provide a high holding torque of 3 N cm at a power of 10.5 W. Smooth operation is obtained by a ramped step rate provided by the Mechanism Controller Board (see Section 13).

8.3. POSITIONING ACCURACY AND FILTER ENCODER

Motor movement is achieved by sequential activation of the 4 motor phases, where two adjacent phases are always simultaneously powered. Each activation step moves the motors by one rotation step. A change to the next filter position requires 27 motor steps in either direction. As the motors do not have permanent magnets (variable reluctance type), they consequently do not have a holding force when not powered. A mechanical locking device is required to keep the filter wheels in place when a filter change is completed.

The filter selection is monitored by a binary system where the code is given by 1–4 SmCo encoder magnets beside each filter and a stationary set of 4 reed switches. The field distribution of the magnets is focussed towards the reed switches thus creating a well-defined activation area.

9. Shutter Mechanism

In each camera an electromechanical shutter in front of the CCD controls the exposure. The shutter is designed to support exposure times between 10 ms and >100 s with a maximum repetition rate of 1 s^{-1}. Typical imaging might use exposure times of 100 ms and repetition rates of one image every 7 s. The shutter is able to expose the 28 × 28 mm^2 active area of the detector with uniformity of better than 1/500. A total of 50,000 shutter operations is anticipated throughout the mission.

The shutter comprises two blades travelling across the CCD parallel to the CCD plane. They are each driven by four-bar mechanisms from brushless dc motors
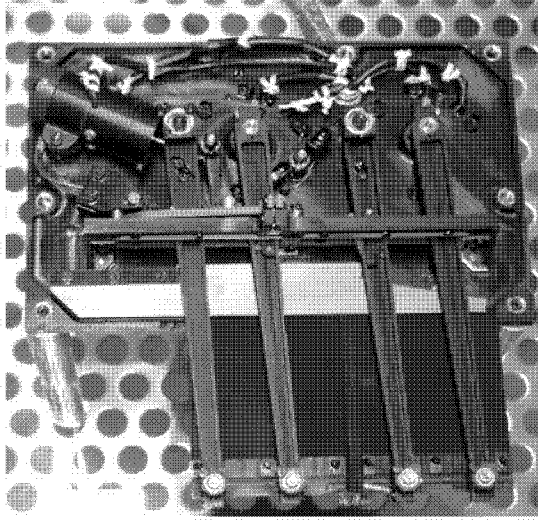
Figure 17. Shutter mechanism flight unit. The shutter blades are at the bottom.

(Figure 17). To determine exposure with high accuracy, a customised encoder for each blade is mounted to the motor shaft.

A position sensor at the final position verifies that the first blade has completed its travel. A mechanical locking device locks the first blade in open position until it is released by the second blade at the end of travel, when the exposure is completed. The back-travel of both blades is provided by springs.

The exposure time is precisely defined by the relative distance (e.g. by the delay) between the moving blades. The exposure time can be any multiple of 0.5 ms, 10 ms minimum.

9.1. BLADE MOVEMENT

The blades are moved in the direction of CCD columns with a constant velocity of $1.3 \, \text{m s}^{-1}$. The blades are accelerated and decelerated by a current waveform controlling the motors in 512 steps each at 8-bit resolution. Figure 18 shows a typical waveform for the actuation of the first blade, which is completed in 53 ms. The blade movement across the CCD lasts 21.3 ms (or $96 \, \text{px ms}^{-1}$).

The blade velocity is measured by an optical encoder mounted on the shaft of the motor. The encoding accuracy leads to a blade position resolution of about 0.08 mm.

9.2. PERFORMANCE VERIFICATION

Uniform exposure across the CCD is achieved by constant blade velocity passing the detector. In order to satisfy the long-term stability requirements, a calibration
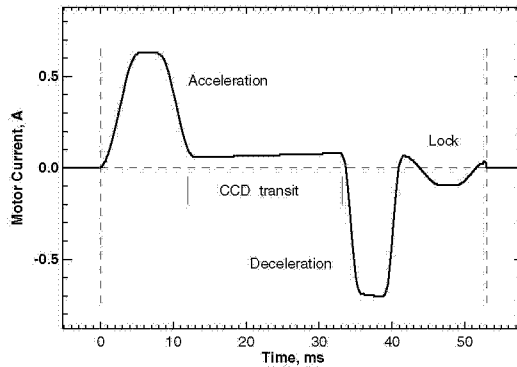
Figure 18. Shutter current waveform to achieve constant velocity across the CCD.

scheme for the shutter blade movement was established. The shutter movement is optimised by adapting the current waveform for the motors by analysis of the encoder data. The Data Processing Unit (Section 12) evaluates the encoder data onboard and generates an optimised waveform in order to achieve uniform exposure of the CCD. A shutter calibration cycle lasts approx. 15 min per camera and is executed routinely in flight.

9.3. SHUTTER ELECTRONICS

The shutter electronics controls the operation of the shutter mechanism. As shown in Figure 19, it is split into a digital and an analogue module. The boards are accommodated in the NAC and WAC CCD Readout Box (CRB box, see Section 11).
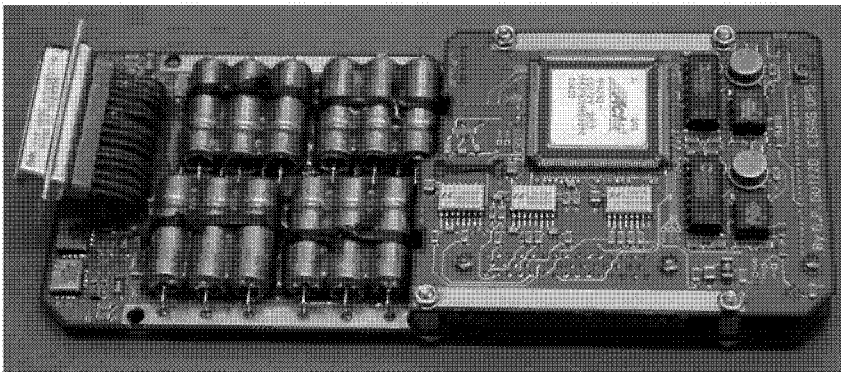

Figure 19. Shutter electronics board.

The digital module stores the current waveform data for both blades in FIFOs. These FIFOs are loaded from the Data Processing Unit with the actual waveform data. Updated waveforms can be calculated onboard or received by telecommand. The waveforms for both blades can be different. The digital module checks continuously the status of the memory and the functionality of the mechanism. The electronics is prepared to identify 11 different types of errors. If an error is detected, the actual status is immediately reported to the Data Processing Unit.

The analogue module is composed of a capacitor bank with associated current switches and the circuitry to select the charge mode for the capacitors. The capacitor bank is needed to feed the motors with a peak power of 20 W during the acceleration and the deceleration phases (10 ms each). Three different charge modes, e.g. fast, nominal and slow mode, are implemented according to the desired shutter repetition time.

9.4. Fail-Safe Mechanism

The fail-safe mechanism configures the shutter into a pseudo frame-transfer CCD mode in case an unrecoverable mechanism failure occurs. It forces the first blade to cover one half of the CCD while the second blade is blocked in the starting position. The open section is then used for imaging. The acquired charge is rapidly shifted into the covered section for intermediate storage and subsequent readout.

10. Front Door Mechanism

The Front Door Mechanism, FDM, is primarily designed to protect the optical components inside the NAC and the WAC by reclosable front doors. The inner side of each door can be used for in-flight calibration in combination with the calibration lamps. The mechanisms for the NAC and WAC telescopes are identical with the exception of the shape of the doors, as these are different in order to fit the entrance baffles of the two cameras. As the front doors cover the field of view of the cameras, the reliability of the entire subsystem during the mission's lifetime requires highest attention.

10.1. Requirements and Design

The main functional and environmental constraints of the mechanism can be identified and summarised as follows:

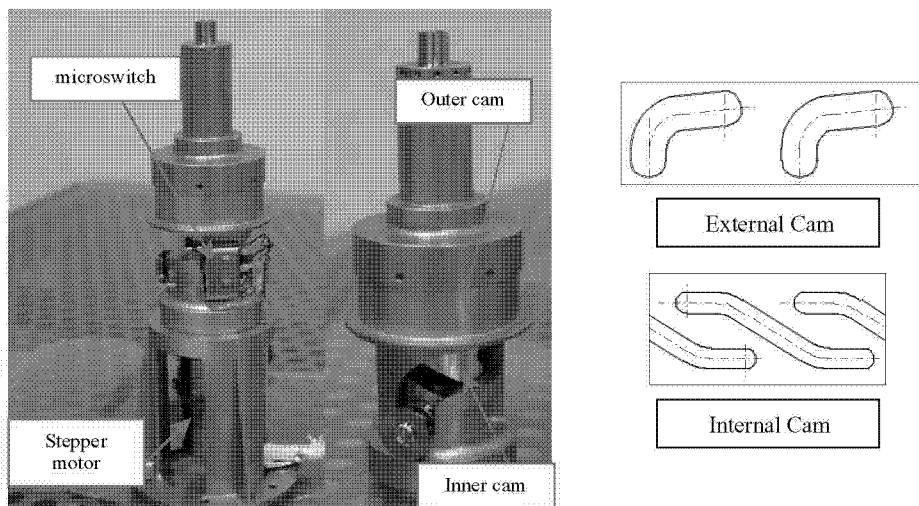- the door has to prevent contamination of the internal surfaces of the telescope

Figure 20. Components of the FDM and cylindrical development of the cams.

- single-point failure tolerance requires redundancy and the ability to open the door permanently in the case if an irreversible system failure occurs (fail-safe device)
- requirement to validate open and closed positions
- dynamic load during launch
- non-operational temperature range $(-50$ to $+70°C)$ implies a design for high differential thermal loads within the mechanisms.

The door mechanism is designed to maintain the moving door always parallel to its closed position plane, thus avoiding direct exposure of the inner surface to open space, to the sun, or to cometary dust particles, because collected contaminants could be re-emitted into the telescope once the door is returned to its closed position. The parallel motion is achieved with two coupled cams that initially lift the door followed by a roto-translation which completes the lift and rotates the door. The shape of the two cams was designed in such a way that both final positions (open and closed) are self-locking states, so that no electrical power is required to maintain these positions, even if the system is exposed to vibrations.

Figure 20 shows the main components of the mechanism generating the movement of the door. The internal cam is activated by a stepper motor with a step angle of $0.3°$ and a gearhead with a reduction ratio of 100:1. The combined motion is transferred to the door by an internal shaft rigidly fixed to the coupling peg and to the supporting arm.

The actual position of the door can be determined from the number of applied motor steps. Nevertheless, two micro switches are employed to identify the open and the closed positions for the housekeeping monitoring. These switches are located on the external cam and are activated by a disk that is fixed on the peg.
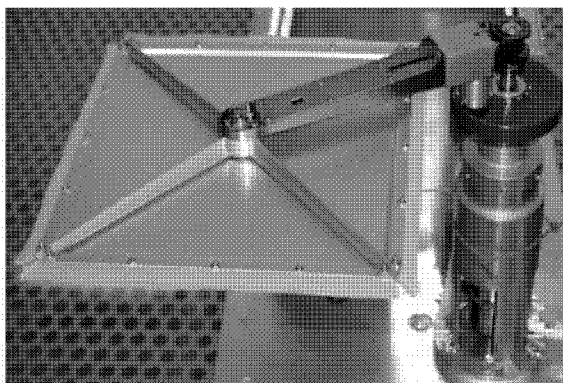
Figure 21. The integrated Front Door Mechanism.

A preload of the door against the external baffle of the camera improves the stiffness of the system composed of the sustaining arm, the door and the external baffle. Potential damage to the baffle due to vibrations of the door, especially during launch, is avoided by a damping seal. Figure 21 shows the completed FDM.

10.2. RELIABILITY

High reliability of the FDM for the extended lifetime of the instrument is of utmost importance. The concept comprises not only redundant drivers and motor windings, but also extensive safety margins in the mechanical design. The latter includes particularly the mechanical load during launch, the specific implementation of sliding parts and, finally, decreased sensitivity to the long-term mission environment.

Differential thermal expansion was taken into account by a number of elastic elements which absorb thermally induced loads. The FDM is covered with a thermal blanket that efficiently isolates the structural parts of the mechanism from thermal paths to the environment.

All moving parts must be coupled tightly together to make the arm stiff enough to sustain the mechanical load during launch. Increased bearing friction by adhesion or cold-welding phenomena must be avoided. Therefore, an innovative lubricant coating has been applied, which relies on the low friction properties of MoS_2, but is not affected by sensitivity to humidity. This so-called MoST coating is a vacuum deposition of MoS_2 in a matrix of titanium that preserves the lubricant properties of the coating.

10.3. FAIL-SAFE DEVICE

A fail-safe device is required beyond the general redundancy concept to make the front door single-point failure tolerant should an irreversible system failure ever occur. This fail-safe device would open the door once and forever.
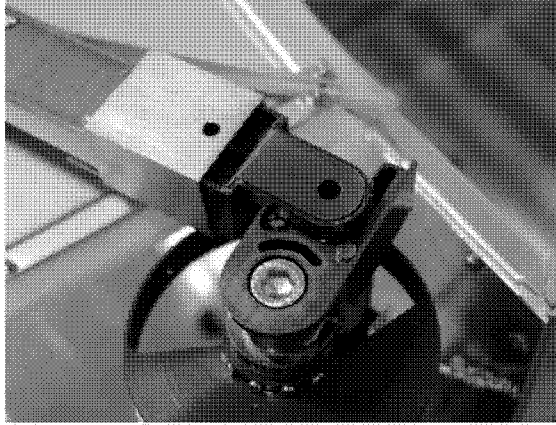
The device is located within the arm holding the door and, to make it fully independent, is operated on an axis parallel to the cam axis. It provides for a lifting of the door and a subsequent rotation of 90° by preloaded springs.

The arm supporting the door has been divided into two parts, which are kept together by a locking slider. The lock can be released by a Shaped Memory Alloy actuator. Once the lock is released and the slider is pulled away by a spring, the arm supporting the door is lifted-up by a coaxial spring. A torsion spring finally rotates the door and keeps the door in the open position. Figure 22 shows the released state of the fail-safe mechanism.

A high preload of 70 N at the main spring was applied to overcome adhesion or cold-welding phenomena, which could appear between the moving parts in the course of a long-term mission. Friction coefficients for the moving parts were minimised also by a sputtered MoST coating on the relevant surfaces of the arm and by a chromium coating deposit on the slider.

11. Image Acquisition System

Both cameras use identical image acquisition systems, consisting of two separate subsystems: (1) the Focal Plane Assembly (FPA), accommodating the CCD detector, the Sensor Head Board (SHB) with the front end electronics, heaters, temperature sensors and radiation shielding, and (2) the CCD Readout Box (CRB box), with the CCD Readout Board (CRB), the Housekeeping Board (HKB), the CRB Power Converter Module (PCM) and the Shutter Electronics (SHE). The FPA and CRB box are about 50 cm apart and are interconnected by a cable of 62 lines.

11.1. Detector Selection Criteria

The detector is a key element of the OSIRIS cameras. Its format and performance have a major influence on the parameters of the optical system. The pixel size determines the focal length for a defined angular resolution, and the QE relates to the F-number. These parameters strongly influence the dimensions of the optical systems. A constraint on the detector selection was the requirement to select a CCD device that needed only little further development for space application saving cost, development time and risk.

The requirement of highest possible QE over the wavelength range from 250 to 1000 nm leads to the choice of backside illuminated CCDs. A minimum pixel capacity of 10^5 electrons was considered as acceptable. Low readout noise in the order of a few electrons per pixel was required to achieve sufficient dynamic range in the image data.

Large CCDs of $2k \times 2k$ pixels have some drawbacks compared to smaller devices. Foremost, they are more sensitive to Charge Transfer Efficiency (CTE) degradations, which occur under high energy irradiation in space. Therefore, tight shielding and the capability to anneal defects at elevated temperatures up to $+130°$C were implemented. The storage temperature of the detectors during cruise is kept near room temperature. A further drawback of the large CCD format is the increased readout time. Two readout amplifiers cut this interval in half and also provide required redundancy.

11.2. OSIRIS CCDs

The OSIRIS CCD design is based on the commercially available, backside illuminated non-MPP E2V CCD42-40 devices with 2 output channels. These CCDs feature the desired pixel size of 13.5 μm^2 and excellent wide-band QE. High dynamic range and low power consumption make them well suited for space applications. The CCD specifications are summarised in Table VII.

The non-MPP clocking register technique yields high full well capacity but also high dark charge generation. Since the dark charge is almost negligible at the in-flight operational temperature range of 160–180 K, the OSIRIS CCD takes advantage primarily of the enhanced charge capacity.

An innovation for the OSIRIS devices was the introduction of lateral (shielded) anti-blooming overflow protection, so that weak cometary features can be imaged near bright regions in long duration exposures. The lateral anti-blooming keeps the entire pixel area light-sensitive so that the QE is not affected. Nevertheless, the full well charge capacity is reduced by the anti-blooming from 140,000 e$^-$ to about 100,000 e$^-$ per pixel.

Dark current becomes a significant component at temperatures above 230 K. Therefore, during the device evaluations at room temperature, full pixel-wide clock

TABLE VII
OSIRIS CCD specification.

Item	Specification
Source detector type	E2V CCD42-40, non-MPP, backside illuminated, Hafnium oxide AR coated
Array size	Full frame, $2k \times 2k$ pixel
Serial register size	$50 + 2k + 50$; 50 extra pixel at both ends $48 + 2k + 48$ transmitted
Pixel size	$13.5 \times 13.5 \, \mu m^2$
No. of outputs	2; either 1 sufficient
Overexposure control	Shielded anti-blooming
Operation modes	Clock dithering for dark current reduction for operations at >220 K (optional), windowing, binning
Full well	$>120\,000 \, e^- \, px^{-1}$
System gain	$\sim 3 \, e^-/DU$
Readout noise (CCD)	$\sim 15 \, e^-$ rms
Dark charge generation	$<0.1 \, e^- \, s^{-1} \, px^{-1}$ @ 180 K $\sim 400 \, e^- \, s^{-1} \, px^{-1}$ @ 293 K – (with dithering)
QE	250 nm: 50%, 400 nm: 60%, 600 nm: 88%, 800 nm: 65%, 1000 nm: 6%
Readout rate	$1.3 \, Mpx \, s^{-1}$; $650 \, kpx \, s^{-1}$ per channel
Readout time (full frame)	3.4 s (2 channels)
Vertical clock rate	$25 \, \mu s$ per line
Operating temperature	$160 \, K < T < 300 \, K$

dithering at a fixed rate of $80 \, \mu s$/cycle was applied, yielding typical dark charge reduction rates by a factor of up to 15. With the help of such dithering, useful images could be obtained up to exposure times of 40 s. Below 230 K, clock dithering is no longer useful, because spurious charge becomes dominant (Kramm and Keller, 2000; Kramm et al., 2004).

11.3. DETECTOR PACKAGING CONCEPT

With high thermal insulation between the CCD substrate and the focal plane housing, the CCD can be operated either at low temperatures (down to 160 K) or can be heated up to 400 K to anneal radiation defects. Special detector packaging was required, therefore, to provide sufficient thermal insulation.

The CCD substrate die is glued to a 10 mm Invar carrier plate that is attached to the housing structure with perfect thermal insulation by two stages of three glass spheres to mount the device (see Section 11.8). Cooling (by a thermal radiator) and (electrical) heating is applied from the back side of the Invar plate. The Invar plate keeps the detector flat to less than 10 μm and provides shielding against irradiation.

The electrical interface is obtained via a small ceramic interface board mounted to the Invar plate. On its top side, the board provides 32 gold plated bond pads, which are aligned with the substrate bond pads on the CCD. A flex circuit connects the CCD to the SHB through gold-plated contacts on the ceramics.

11.4. READOUT CONCEPT AND IMAGE FORMATS

In stand-by mode, the CCD is continuously clocked at a moderate rate of about 3 ms/line. Prior to an exposure, the CCD is entirely cleared by a fast vertical dump of 25 μs/line. The exposure is started by the shutter opening and completed by the movement of second shutter blade.

Full frame or sub-frame (window) images can be read with or without binning and via either one or both channels. If both channels are used to read a sub-frame of the CCD, the centre of the sub-frame must be aligned with the centre axis of the CCD. Binning formats of 2×2, 4×4 and 8×8 pixels are supported.


11.5. SENSOR HEAD BOARD

The sensor head provides only limited space for electronics. As a consequence, the front-end electronics accommodate just the preamplifiers and protection circuitry. This concept minimises the power dissipation in the FPA section and thus protects the CCD detector from heating up. The total power loss in the FPA section is made up of approximately 90 mW within the CCD substrate and about 270 mW on the SHB.

11.6. CCD READOUT BOARD

Each CRB contains two complete signal chains, including line receiver, the correlated double-sampling (by clamping), the buffer amplifier and analogue-to-digital converter (ADC). All clock signals are provided by an ACTEL 1280 Field Programmable Gate Array (FPGA). A second FPGA handles the high speed serial (LVDS) data link to the DPU.

The implementation of the ADC section was complex because the required data resolution of better than 14 bit could not be achieved with a single ADC in each channel. A sub-ranging technique was applied using two simultaneously operated 14-bit ADCs in each channel, one for the range up to $50,000\,e^-$ and the second covering the range up to $200,000\,e^-$. The criterion for the selection of the conversion result is based on the occurrence of an overflow at the low-range converter. We selected the LTC1419 type ADC because it was found to be radiation resistant to at least 50 krad (Tomasch *et al.*, 2000).
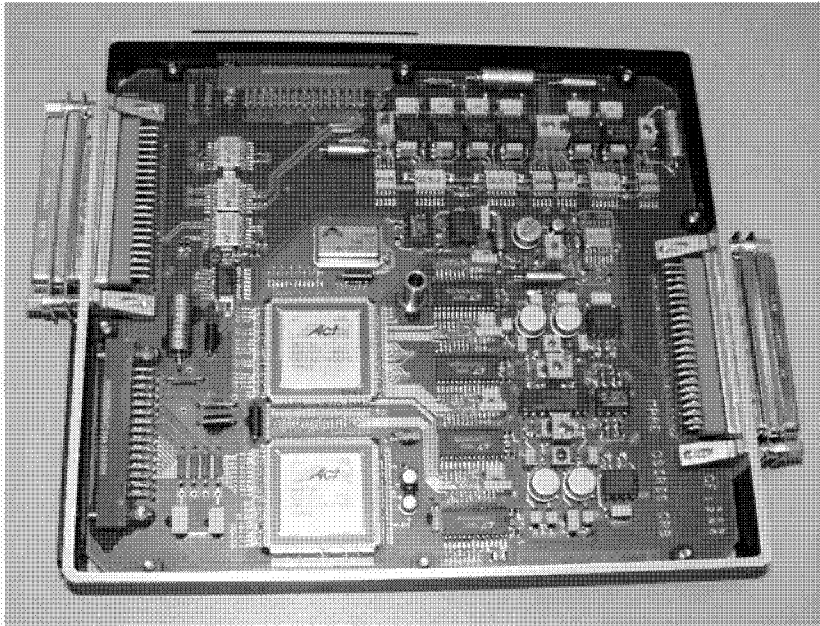
Figure 23. The CCD readout board.

The entire readout electronics could be accommodated on one board with the help of four different types of thick film hybrid circuits especially designed for OSIRIS to save both space and power (Figure 23).
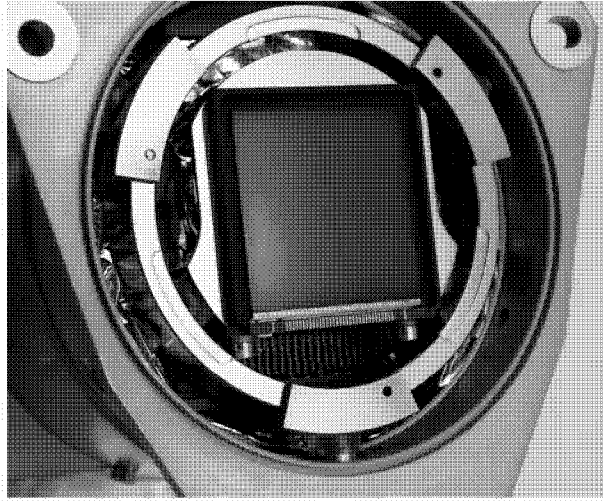
About 1.6 W are sufficient for stand-by operation, and 3.2 W are required during readout.

11.7. HOUSEKEEPING BOARD

The operating conditions of the CCD, the FPA and the CRB are monitored by the HKB. It measures the voltage and current on all six power lines, and determines the temperatures of the CCD, the shutter actuators, the ADCs and the related PCBs. Furthermore, the HKB reads the dosimeter-FET that was implemented to track the camera total ionizing dose. All housekeeping data are incorporated in the image header. The HKB requires less than 190 mW.

11.8. FPA MECHANICAL DESIGN AND THERMAL CONTROL

As shown in Figure 24, the Invar plate carrying the CCD substrate die is thermally insulated by two concentric groups of three glass spheres. A titanium ring in-between holds the glass spheres in place and serves as an additional insulator.

The thermal resistance between the Invar plate and FPA housing is in the order of 500 K/W.

A cold finger connects the Invar plate to a radiator for passive cooling. The thermal conductivity of the cold finger is a trade-off between two contradictory requirements. Operating the CCD requires low gradients between the radiator and the CCD. On the other hand, annealing the CCD with limited heater power requires a considerably higher gradient on this path. Developing a 'thermal switch' between the radiator and the CCD would have been an elegant solution but was judged to be a technological risk and thus was rejected. The compromise is a cold finger consisting of 45 single aluminium sheets of 0.1 mm thickness. The temperature gradient between the radiator and CCD during operational conditions is in the order of only 1 K. The lightweight radiator is mechanically mounted to the FPA housing by a supporting structure of 7 GFRP (glass fibre reinforced plastic) tubes (Figure 25).

The total conductive and radiative heat input onto the cold parts from the warm FPA housing, from the telescope in front of the CCD and from the SHB electronics sums up to nearly 1 W. To reach the nominal operating temperature of 160 K, a radiator surface of 430 cm^2 is needed. The radiator has a view factor of nearly 2π sr to deep space. Its outer surface is painted with a conductive white paint having a low solar absorption coefficient α and a high infrared emissivity ε. The low α helps to reduce the heat input and temperature changes of the CCD during asteroid flyby phases, when sun incidence on the radiator cannot be avoided.

The CCD temperature is passively controlled by the efficiency of the radiator, but it can be adjusted electrically by 4 heaters mounted to the cold inner parts. A 0.5 W heater is used to adjust the operating temperature to levels higher than defined
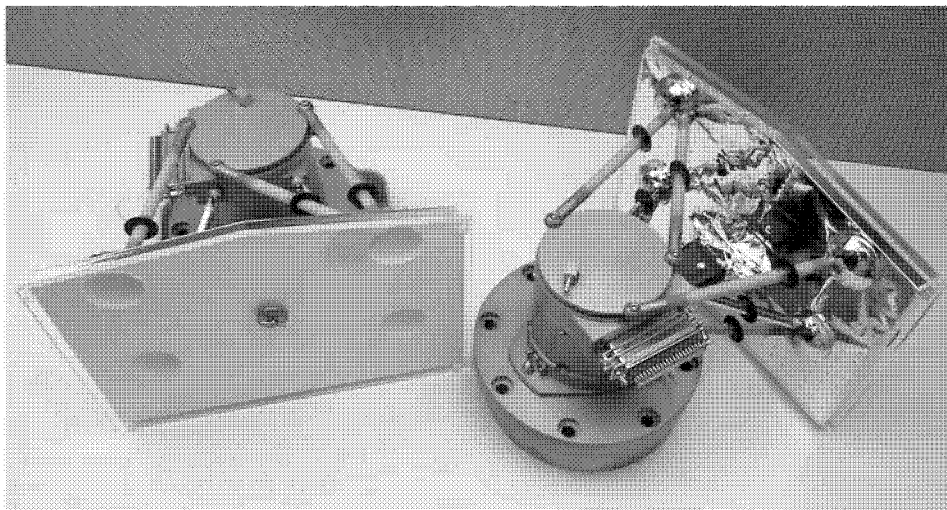
Figure 25. NAC and WAC focal plane assembly.

by the passive cooling. Two 3 W heaters are powered by the spacecraft during non-operational phases to keep the CCD at elevated temperatures and minimise radiation damage effects. A 25 W heater is installed to decontaminate and anneal the CCD.

11.9. RADIATION PROTECTION

Solar protons dominate the radiation effects to the CCD in the inner heliosphere. They generate lattice defects at a sensitivity threshold of a proton fluence of $10^8 \, \mathrm{cm}^{-2}$ or a dose equivalent of 100 rad (Holland et al., 1990). Passive shielding of the CCD was implemented in both cameras to ensure high performance at maximum solar activity after 9 years cruise.

Dense absorbers and a dedicated quartz window plus the optical filters in front of the CCD reduce significantly the number of incident protons. However, radiation shielding to $20 \, \mathrm{g} \, \mathrm{cm}^{-2}$ or 150 MeV kinetic energy is required for appropriate reduction of the proton fluence for the Rosetta mission.

Mass and volume restrictions do not allow full implementation of shielding. Additional measures were taken to ensure a CTI (*C*harge *T*ransfer *I*nefficiency) at levels better than 2×10^{-5}. Raising the CCD temperature to near room temperature during cruise reduces significantly the damages by long-term annealing (Hopkinson, 1989). Additional annealing at elevated temperature up to $+130°$C will remove accumulated degeneration up to 85% (Abbey et al., 1991) but is limited due to high mechanical risks and stress at the CCD.

Thus, the OSIRIS CCD radiation protection is designed to an accumulated proton fluence of $10^9 \, \mathrm{cm}^{-2}$ with passive shielding to a minimum of $5 \, \mathrm{g} \, \mathrm{cm}^{-2}$ or 70 MeV

equivalent. Heaters ensure long-term and high-temperature annealing during the mission and stacking of low and high-z absorbers along the particle track reduces x-ray and neutron generation inside the shielding (Dale, 1993). The nominal CCD operational temperature (160 K) will freeze out traps caused by residual lattice defects and enlarges the emission time constant. CTI verification in flight will allow real-time determination of defects.

Radiation effects were studied on two OSIRIS CCD samples that were exposed to 10 and 60 MeV proton irradiation up to a fluence of 2×10^{10} cm^{-2}. We found that long-term room temperature annealing significantly reduces the increased dark charge leakage, while high temperature annealing is particularly suitable to cure degraded CTE (Kramm *et al.*, 2003).

12. Data Processing Unit

12.1. ARCHITECTURAL DESIGN

The main driver for the design of the OSIRIS Data Processing Unit (DPU) is the need to control camera operations as well as to acquire and process image data from the two CCD arrays. This made a Digital Signal Processor (DSP) desirable. The DPU is based on a development of the ESA Technical Directorate using the radiation-hard version of the Analog Devices ADSP21020 processor.

Because of power limitations, the speed of the processor had to be substantially reduced. A large local memory was implemented so that extensive processing tasks could be executed by batch processing rather than in real-time. This scheme does not impose a significant limitation to the operations, because the data transmission rate is the most restricting requirement.

The DPU architecture is driven by the following requirements:

- high data rate from both cameras operated simultaneously (up to 40 Mbit s^{-1})
- output data rate (to spacecraft mass memory, SSMM) limited to 10 Mbit s^{-1}
- support of 'movie' operation (up to 64 images with ~1 s image repetition time)
- single-point failure tolerance
- limited resources of mass and power
- decision to base the architecture on an existing TSC21020 processor board.

The discrepancy between the input and output data rate necessitated a DPU internal storage of minimum one WAC and one NAC image. The data transfer rate to ground is limited to 100 Mbit/day. Image transfer rates can be increased by image compression at the expense of image fidelity. State-of-the-art (lossy) wavelet compression with a compression ratio between 4 and 8 provides the best balance between image degradation and a substantially increased image count. For

the observation of dynamic events, the optimum balance is expected to require even higher compression factors.

Compression can be performed either in real-time (in step with the incoming camera data) or by intermediate storage and subsequent processing of the stored raw data. The latter was implemented because the limited bandwidth of the telemetry restricts the time for image acquisition but leaves time for software compression.

12.2. IMPLEMENTATION

The DPU block diagram is shown in Figure 26. The DPU consists of four elements each mounted in one mechanical frame of the Electronics Box (E-Box, see Figure 5):

- Main Processing Element (PE), consisting of the processor board with the DSP, local memory, spacecraft interface, and internal IEEE 1355 interfaces, and a memory extension board
- Redundant Processing Element in cold redundancy
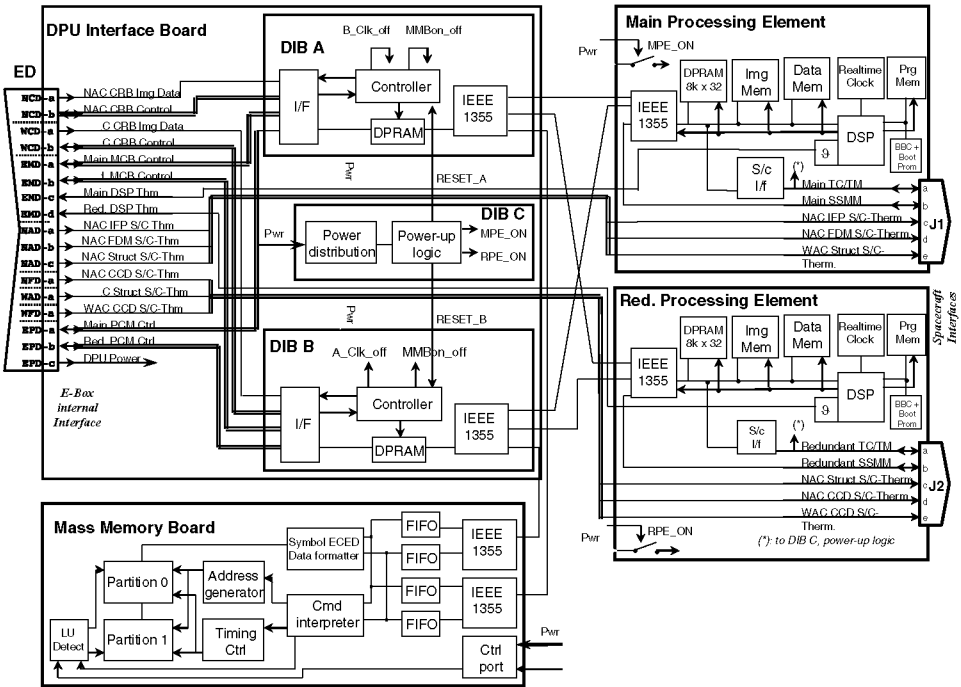- Mass Memory Board (MMB), containing 4 Gbit of image memory, control logic, and IEEE 1355 interfaces

Figure 26. Block diagram of the OSIRIS DPU architecture.

TABLE VIII

DPU characteristics.

Item	Specification
Central microprocessor	Rad-hard Temic processor based on Analog Devices ADSP21020, 20 MHz, 60 MFLOPS, data transfer from local memory to mass memory 38 Mbit s^{-1}
Mass memory	4 Gbit net
Program memory	8 kbyte (8 bit) PROM (bootstrap kernel)
	256 kword (48 bit) E^{2}PROM (OS, task-specific program modules)
	256 kword (48 bit) program SRAM All program memory latch-up and SEU immune
Local data memory	4 Mword (32 bit) fast SRAM for local image storage
	128 kbyte non-volatile E^{2}PROM
	128 kword (32 bit) fast SRAM for stack/variables storage (zero wait state, latch-up and SEU immune)
Digital interfaces	Serial command interface to NAC CRB and WAC CRB
	Serial data interface to NAC CRB and WAC CRB
	Serial command and data interface to MCB
	Serial command and data interface to PCM
	Spacecraft interface IEEE 1355 interface to SSMM
Redundancy	Processing Element, spacecraft interface: dual cold redundant MMB: graceful degradation
Protection against single event errors	SEL: latch-up detectors (MMB only)
	SEU: memory error correction, SSCDSD (MMB only)
	DSP watchdog
Power management	Nominal and low power mode, implemented by: (a) program SRAM deselect, (b) clock disable of DIB A or DIB B, c) MMB switch-off
Operating system	Real-time operating system (Virtuoso)

- DPU Interface Board (DIB), with the power-up logic, the interfaces to the NAC CRB, WAC CRB, MMB, Mechanism Controller Board (MCB), Power Converter Module (PCM), and IEEE 1355 interfaces.

An overview of the DPU performance characteristics is given in Table VIII. The unfolded DPU flight unit in a test configuration with a prototype of the MMB is shown in Figure 27.

12.3. PROCESSING ELEMENT

The two PEs of the DPU are identical and cold redundant. The activation of the selected PE is done during power-up of the DPU by the telemetry sample signal.
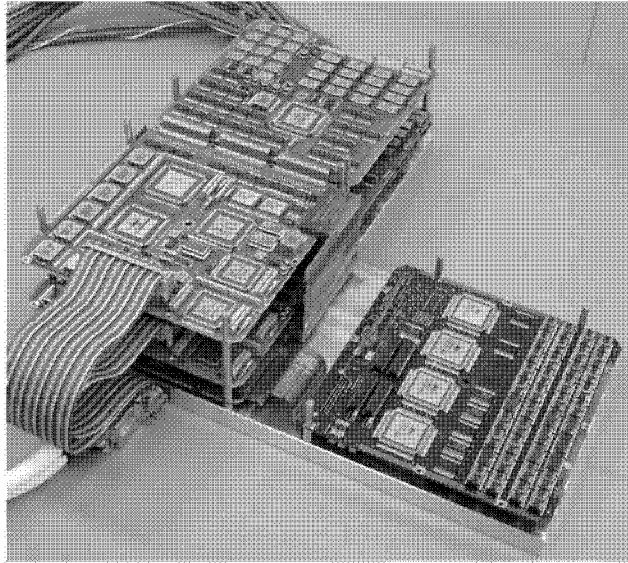
Figure 27. DPU FM under test with a prototype of the Mass Memory Board.

Each PE is implemented on two printed circuit boards and provides:

- TSC21020F 32-bit floating point digital signal processor clocked at 20 MHz
- 1.5 Mbyte of zero wait state program memory
- 512 kbyte of zero wait state data memory
- 16 Mbyte image memory on the extension board
- 1.5 Mbyte E^2PROM for non-volatile program and data storage
- 128 kbyte E^2PROM for non-volatile parameter storage
- 32 kbyte dual port communication memory
- 3 IEEE 1355 high-speed communication links
- SMCS332 communication controller
- TM/TC (telemetry/telecommand) interface controller.

The processing performance of the DPU allows wavelet image compression of a $2k \times 2k$ image in less than 50 s at a compression ratio of $c = 12$ and in less than 30 s of a 1024×1024 image at $c = 4$ by using an optimised assembler code (Christen *et al.*, 2000).

12.4. MASS MEMORY BOARD

The MMB provides a user capacity of 4 Gbit, which is implemented in 4M4 DRAMs, 4-high stacks of 64 Mbit capacity each. The memory is protected by an extended (80, 64) Reed-Solomon code against single 4-bit wide symbol errors. The array is split into 2 partitions. A partition is composed of 8 word groups, each

of them containing 4 Mword of 80 bits, which are accommodated in twenty DRAM chips.

The word length of 80 bits is structured into 16 data symbols and 4 parity symbols. The code is capable of correcting errors in one symbol of 4 adjacent bits and of detecting errors in 2 of such symbols (Fichna *et al.*, 1998). The address management provides logical addressing of the configured memory space in terms of active word groups, start address and block length.

Data integrity is provided by background scrubbing for Single Event Upset (SEU) error removal. Overcurrent sensors and circuit breakers in the supply lines protect each partition individually from Single Event Latch-up (SEL) events.

The MMB has dual redundant communication interfaces and two independent partitions. In case of a failure in one partition, this partition can be switched off (graceful degradation). The processor workspace can store and process a complete raw image in the absence of both partitions of the MMB. The MMB communicates via two differential IEEE 1355 serial interface links, each providing simultaneous data transfer of 38 Mbit s^{-1} in both directions. All peripheral functions of the module are accommodated in Actel 1280 FPGAs. Each FPGA includes functions for enhanced SEU tolerance.

12.5. REDUNDANCY CONCEPT

The DIB is split in two identical parts interfacing the cameras: DIB A for the NAC and DIB B for the WAC. In consequence, the two camera chains (CCD detector – CRB – DIB) are redundant. The PEs are cold redundant. The two PEs and the two camera chains are cross-strapped using the capability of the IEEE 1355 ASICs to accept three interfaces.

13. Mechanism Controller Board

The Mechanism Controller Board, MCB, drives the motors of the front doors and of the two filter wheels in both cameras (see Section 8). The four-phase dual-step, variable reluctance stepper motors were built with redundant windings, which can be powered alternatively or in parallel. The MCB also acquires housekeeping data from the position encoders on the front doors and filter wheels and from the temperature sensors of the two cameras.

13.1. MCB DESCRIPTION

The MCB consists of two boards, the Control Board and the Drivers Board, both mounted into the E-Box MCB frame (Figure 28). They are interconnected via two flexible, low profile boards (Sferflex technology). Connections to the cameras are provided via 62-pin connectors. Communication with the DPU is established via RS-422 type line drivers and receivers.
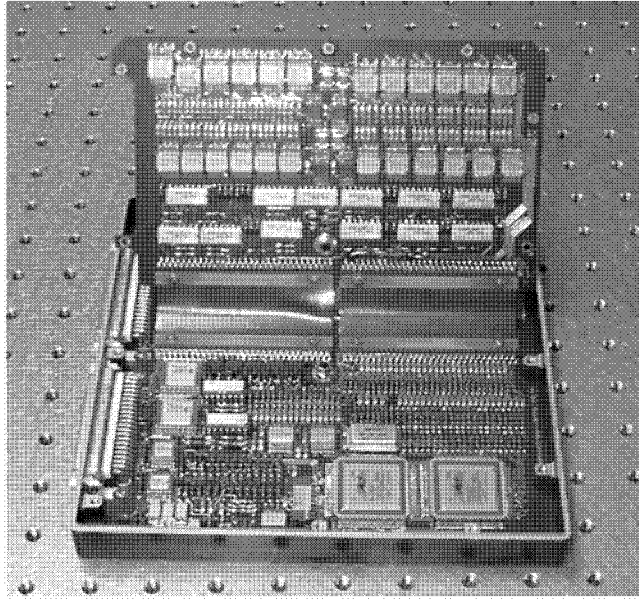
Figure 28. The mechanism controller board.

The Control Board hosts the digital circuitry for communication and mechanism control and the analogue housekeeping acquisition. The digital functions are concentrated in two FPGAs performing the command decoding, the data collection, the packaging and the data transmission. They also translate the DPU mechanism commands into motor phase pulses that are transferred to the Drivers Board. Full dual redundancy was established for the line drivers and for the digital and analogue conversion circuitry. The main and the redundant analogue data acquisition modules can read the temperature sensors regardless of which stage is in use. Similarly, both main and redundant modules can read the position encoders of all mechanisms.

The Drivers Board accommodates the motor drivers. As each camera unit contains three motors, 48 line drivers are required to feed the main and the redundant phases of all motors. Driving the motors directly from the +28 V spacecraft primary power rail requires electrical isolation of the motor switches from the remaining electronics by optocouplers.

13.2. CONTROLLER FPGA

The Controller FPGA establishes the communication, the command decoding and execution, the housekeeping data acquisition and the reset functions.

The communication link to the DPU uses standard RS-422 interfaces, one in each direction. Each transferred byte is 8 bits wide with 1 start bit, parity even and 1 stop bit. A communication packet consists of one command or packet identification

byte and of an appropriate number of parameter bytes (0–5 bytes on receiving, 3–87 bytes when transmitting). Each packet is finally terminated by a checksum byte.

The command decoder interprets the received commands. Commands are related either to the data acquisition, to the stepper controllers or to the parameters of the 6 motors, i.e. phases and step pattern. Each command is approved for coherence and possible transmission errors in parity, frame or checksum. Motor control commands are forwarded to the Controller FPGA. Invalid commands are rejected, and an error flag is returned in the status word.

The MCB recognises two types of reset signals, the (internal) power-on reset and the system reset command from the DPU. Both resets re-initiate the MCB to the default parameter set.

13.3. STEPPER FPGA

The Stepper FPGA consists of three blocks:

- controller block containing two independent controllers to allow simultaneous operation of two motors with independent parameters
- motors block providing the generation of phases to the motors, with the option to define the initial phase of movement
- communication block for the interface to the controller FPGA.

The program repertory includes parameters for the minimum (first and last step) velocity, for the maximum velocity, for the acceleration and the deceleration ramps and for the total number of required steps. An example for a nominal ramping profile for a single filter change is provided in Figure 29.
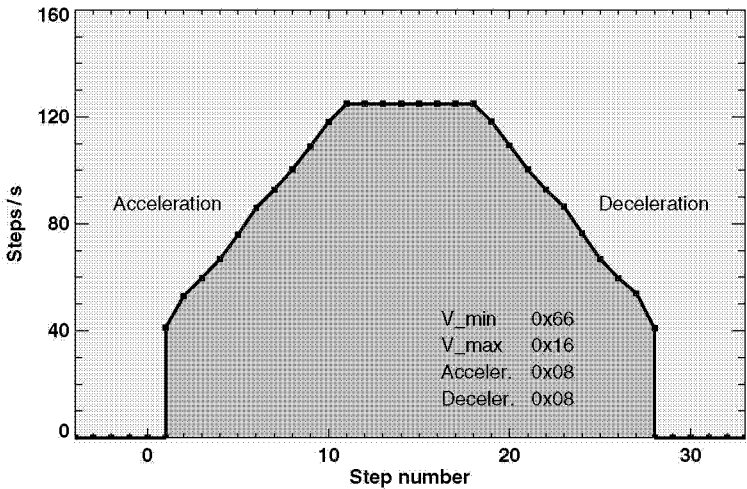

Figure 29. Nominal ramping of the motor step frequency.

The stepper motor controller keeps the final phase powered for a holding time of 463 ms to obtain high position accuracy in deceleration. Another important functionality of the MCB is the warm-up of the motors and its mechanisms by powering individual or dual windings. The power command in heating mode must be repeated once a second until the envisaged heating effect is achieved.

14. Power Converter Module

The Power Converter Module, PCM, provides power for the OSIRIS instrument. High conversion efficiency is achieved with a regulated switching DC/DC converter technique. Unused instrument subsystems can be switched-off by solid-state relays. Distribution of noise is substantially reduced by filtering and isolation.

The initial idea was to use a central power converter unit for the entire instrument. During the development, the power conversion tasks were split into a main PCM and small dedicated converters close to the CCD Readout Boards to reduce the risk of noise pick-up. Thus, the PCM is comprised of a module in the lower compartment of the E-Box, and the NAC CRB PCM and the WAC CRB PCM, which are located in the respective CRB boxes. E-Box PCM-to-DPU communication is provided via standard bi-directional RS-422 serial interface links.


14.1. E-Box PCM

The E-Box PCM is accommodated on two boards of $190 \times 190 \, \text{mm}^2$, namely the Power Control Board and the Power Distribution Board (Figure 30).

The Power Control Board hosts the digital circuitry that performs primarily the following tasks:

- execution of commands from the DPU, e.g. the distribution scheme for primary and secondary power or requesting housekeeping data, supported by redundant microcontrollers
- generation of control signals to the switches and latching relays on the Power Distribution Board
- collection and transmission of housekeeping data from the Power Distribution Board
- determination of the primary current limitation threshold. The threshold can be modified according to actual operational modes.

The Power Distribution Board contains the power units and analogue circuitry:

- main and redundant DC/DC power converters to feed the DPU, the MCB, the PCM, and other consumers such as lamps, heaters etc.
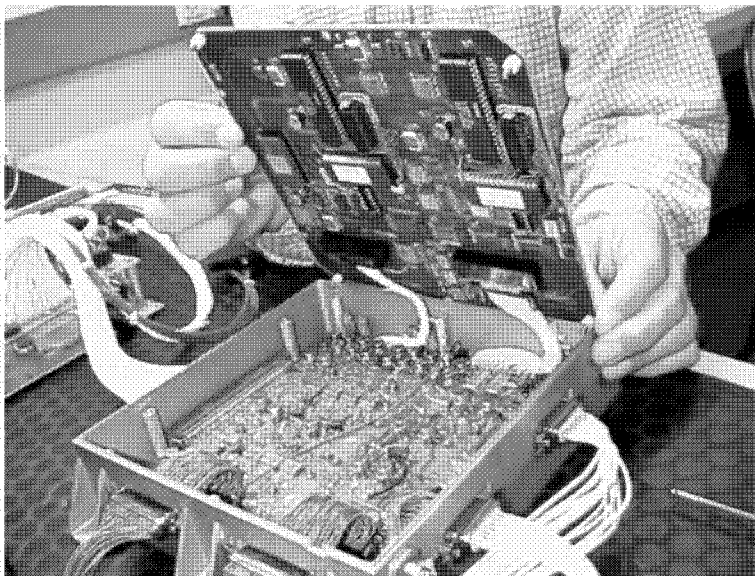
*Figure 30.* Bread-board model of the E-Box Power Converter Module.

* power distribution as requested from the Power Control Board
* acquisition of associated housekeeping data.

The Power Distribution Board receives the main and redundant primary power lines through separate connectors. The entire power conversion stage, consisting of the EMI filter, the inrush control circuitry and the DC/DC converters, is established with full redundancy. The following power distribution stage (including the inrush current control as well as the slope and delay control of the secondary voltages) distributes the secondary power to the shutter electronics, to the MCB and other consumers. Solid-state relays and optocouplers are used where necessary.

14.2. PCM SOFTWARE

The onboard PCM software is stored in an 8-kbyte-wide PROM. The PCM software has the following autonomous functions:

* supervision of the state of the non-active (redundant) microcontroller
* detection of a primary current limit violation
* detection of a housekeeping limit violation
* detection of Single-Event Upset.
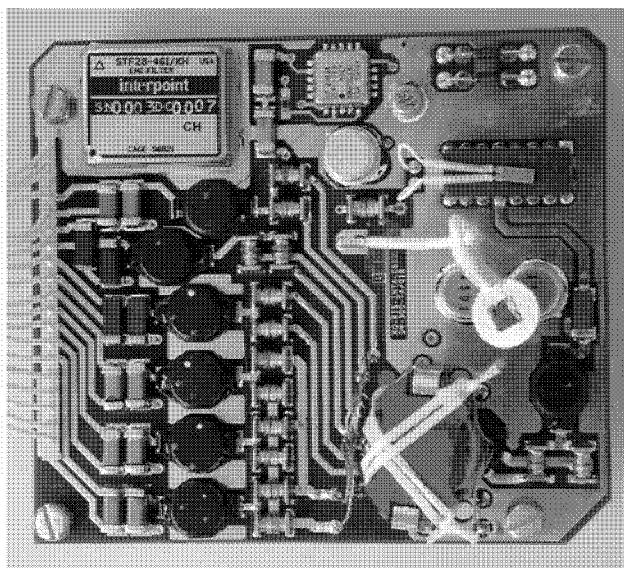
Figure 31. Power converter module for the CCD readout board.

Limit overruns are reported to the DPU and, if necessary, endangered subsystems are disconnected autonomously by the PCM software.

14.3. CRB PCMs

A CRB Power Converter Module (CRB PCM, see Figure 31) is located in each of the two CRB boxes. It provides six supply voltages for the detector electronics, the housekeeping board and operational heater at the CCD.

The CRB PCM provides electrical isolation from the spacecraft primary power bus. It is based on a regulated switching DC/DC converter with high efficiency. Minimisation of conducted EMC, emission and susceptibility is achieved by EMI filters and snubbers at the switching stage of the converter.

Due to the sensitivity of the analogue signal chain to external noise, converter switching was synchronized with the pixel readout. The CCD Readout Board provides the synchronization signal to the converter. The phase of this so-called 'Sync Pos' signal can be shifted by one of 32 possible incremental steps relative to the pixel readout period to achieve operation with lowest noise pick-up. If, however, the synchronization signal is not available, the CRB PCM operates in free-running mode. In nominal operation, this condition occurs only during power-on when the circuitry for synchronization signal is not yet settled.

15. Onboard Software

The OSIRIS flight software is composed of three sections:

- kernel software
- OSIRIS UDP library
- OSIRIS science library.

15.1. KERNEL SOFTWARE

The kernel software provides the low-level functionality of OSIRIS, e.g. the TM/TC interface and the hardware drivers. A novel concept of onboard operational procedures was implemented for instrument control, image acquisition and process sequencing. The OSIRIS Command Language (OCL) is a systematic approach to generate or to adapt onboard application software for instruments with varying operational profiles during mission. It continues and extends previous approaches, as e.g. applied in SOHO/SUMER by Kayser-Threde (Birk, 1992). OCL comprises a middleware-system for (1) application layer functions with operational sequences in a high-level language (so-called User Defined Programs, UDPs, and Persistent Operational Programs, POPs), (2) upload of UDPs, and (3) onboard script execution, supported by virtual machines which interpret the precompiled scripts. Software integrity is supported by onboard checks as well as by language-inherent features.

The architecture of the OSIRIS OCL system is shown in Figure 32. It consists of a space segment with the UDP manager and virtual machines, and a ground segment with a compiler to generate UDP token code including a translator to convert the code to a series of telecommands. The UDP manager handles the UDP code onboard. The token code can be stored in memory or transferred as POPs to non-volatile RAM. UDPs are invoked either by the UDP manager directly or via a timeline.

The structure of the OSIRIS flight software is outlined in Figure 33. The UDPs represent the upper layers (application layers). OCL is located at the mid-layer (level 4) in the software architecture.

The major functionalities of the five software layers are:

- level 4: the token interpreter executes POPs and UDPs. UDPs can call functions in the low-level kernel software (the run time library) or call other UDPs. The UDPs are executed from ground using an execute-by-name scheme (with parameters)
- level 3 contains library functions such as image acquisition and basic image processing. It contains a library of image evaluation functions, like
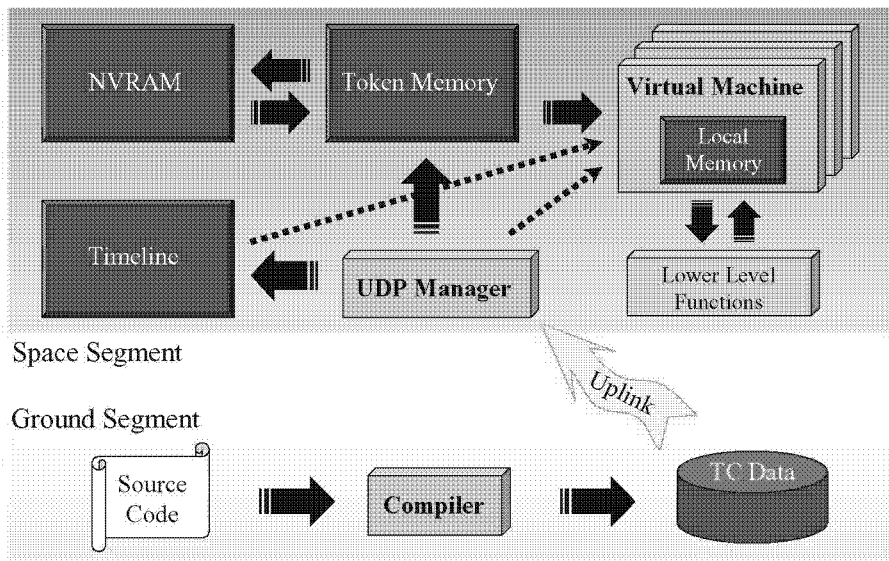
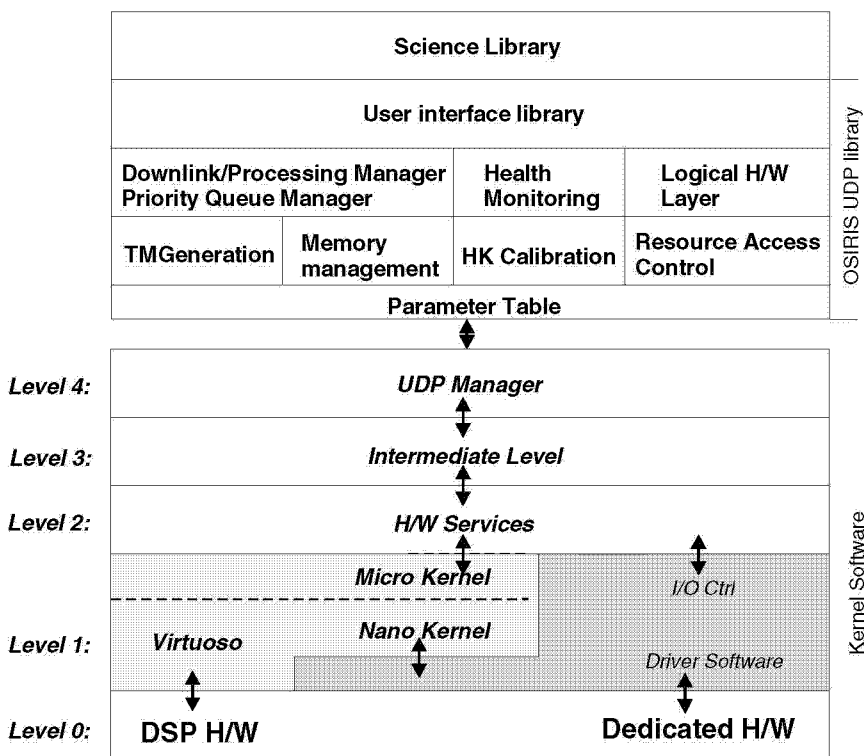*Figure 32.* Architecture of the OSIRIS command language system.

Figure 33. Structure of the OSIRIS flight software.

histogram, sub-framing, binning, bright point determination, and the SPIHT (Set Partitioning In Hierarchical Trees) wavelet-based image compressor supporting lossy and lossless compression

- level 2 interfaces to the Run Time Operation System, RTOS, and the driver software. It consists of service functions to the serial devices of NAC, WAC, MCB and PCM and to the MMB. Telemetry, telecommand and the IEEE 1355 interfaces to the SSMM are served. All software interfaces above this level are hardware independent

- levels 0 and 1 interface the DPU hardware with the next higher software level. Level 0 consists of hardware descriptions, like address, port, and data definitions. Level 1 is shared by the RTOS Virtuoso (Eonic Systems) and driver software. RTOS interacts with processor devices. The drivers serve dedicated hardware. The boot loader program can load program data from the internal E^2PROM or from the spacecraft mass memory via the IEEE 1355 interface.

The kernel modules and the data flow are shown in Figure 34. Interconnections between the modules are made in different ways, depending on data and command flow. Data driven program parts use Virtuoso mailboxes, Virtuoso FIFOs (on a single word base), as well as Virtuoso events (one-bit information used by driver software) to communicate with other modules.

Figure 34. Interaction between software modules within OSIRIS.

Maintainability of the OSIRIS DPU software is guaranteed by a typical set of programming conventions (naming conventions, header format and commenting rules, etc.), revision control and back-up strategies.

15.2. OSIRIS UDP LIBRARY

The OSIRIS UDP library is a collection of routines written in OCL language. The library provides an interface between the scientific users of OSIRIS and the hardware specific details required by the kernel software. The following modules exist (see Figure 33):

- management of the parameter table. This module handles the modification and dump of the parameter table via the TM/TC interface and persistent storage of the parameters in the OSIRIS non-volatile memory
- the resource access control module protects resources to be accessed by parallel running UDPs
- OSIRIS image and data memory is accessed via the memory management module
- a telemetry generation module implements the high-level protocol for message events, generic data dumps and image data transfer
- downlink is managed by a module providing downlink prioritization via a number of queues
- the hardware abstraction layer (logical H/W layer) allows the user to command the hardware modules using logical parameters, e.g. move filter wheel to a specified position instead of turn filter wheel a number of steps in a given direction, and provides calibration of all HK channels
- health monitoring is provided by real-time monitoring of OSIRIS and will safeguard the instrument in case of anomalies. All currents, voltages, and temperatures are monitored as well as the radiation environment via data from the SREM radiation monitor onboard Rosetta
- a module providing self test and performance tuning functions.

15.3. OSIRIS SCIENCE LIBRARY

The OSIRIS science library is a collection of UDPs that implement complex scientific observations as single commands. Various multi-spectral sequences are implemented, where full spectral cubes can be acquired. The point of the scientific UDP library is that the library can easily be expanded to serve future needs of both simple serial activities and highly complex activities requiring onboard intelligence and data processing. An example of a proposed UDP is an onboard cometary outburst detector that periodically acquires images and only downlinks the data if brightening of the comet is detected.
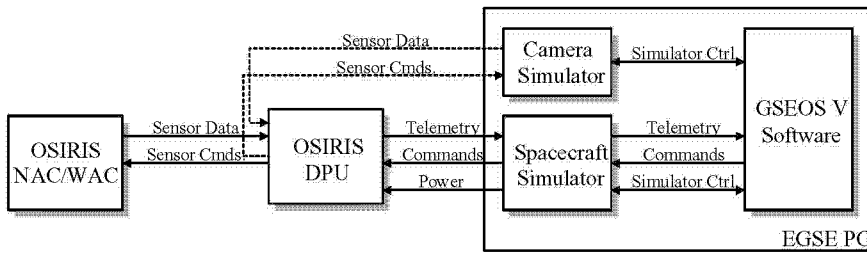
Sensor Data
Sensor Cmds

Camera Simulator Simulator Ctrl

GSEOS V Software

OSIRIS NAC/WAC — Sensor Data / Sensor Cmds — OSIRIS DPU — Telemetry / Commands / Power — Spacecraft Simulator — Telemetry / Commands / Simulator Ctrl

EGSE PC

Figure 35. Commanding concept for the OSIRIS EGSE.

16. EGSE and Telemetry

16.1. EGSE AND ASSOCIATED SOFTWARE

The OSIRIS Experiment Ground Support Equipment (EGSE) consists of a standard PC equipped with subsystem simulators providing all interfaces for ground testing as well as for flight operations (Figure 35). Hence, the EGSE supports the entire instrument development and maintenance and also provides quick-look presentations and health monitoring.

The operating software is based on the software package GSEOS V running on Windows XP. GSEOS V supports the tests of the instrument under near-real-time conditions. A data-driven concept is used instead of less efficient polling. GSEOS V is configured for OSIRIS using the built-in G-compiler, which is based on the C language and is enhanced in some properties to support the data-driven concept.

GSEOS V provides numerous functional modules:

- commands can be sent to the instrument directly or via network; manual, time-tagged or event-driven commands are accepted
- instrument data are grouped into blocks (e.g. science or housekeeping data). Blocks are user-defined structures on the bit level. Data processing is data driven; if a data block is received, the decoder module calls the related, user defined function for processing
- instrument data can be displayed in various formats (hex, decimal, text, bitmap, histogram, plot)
- data can be checked and evaluated; if a limit is exceeded, a user-defined reaction can be activated (e.g. power off, print of an error log)
- command, status and data protocol logging
- incoming and outgoing data can be saved on disk and can be replayed
- the EGSE can be connected to the network on an IP level. All program functions are accessible via the network. Special communication protocols (e.g. CCSDS, SFDU) are implemented.

16.2. TELEMETRY CONVERSION

The DPU acquires the image and associated housekeeping data, performs pre-processing (compression) if required and provides the packaging for the telemetry. The information about the processing steps is attached to the telemetry so that the data can be reconstructed on ground.

When the telemetry data are received on ground, the images and their headers are extracted and recovered from the data stream. The binary telemetry header is converted to ASCII format and finally stored with the image data in individual files.

The data archiving is organised by the OSIRIS software written in IDL. A software library retains routines for reading, writing, and processing the OSIRIS image data. The files are stored in eXternal Data Representation (XDR) format. PDS (Planetary Data System) formatted data are generated as well.

17. Calibration

17.1. GROUND CALIBRATION

The OSIRIS system was calibrated in several stages. Prior to final system integration, the NAC underwent a series of unit tests at LAM in Marseille to verify focus, thermal stability, stray light performance, geometric and absolute calibration. At UPD, the WAC underwent a series of focus tests. After mating with the flight electronics at MPS, a further series of calibration tests was performed at system level (Figure 36): focus, flat-fielding, spectral response (including temperature
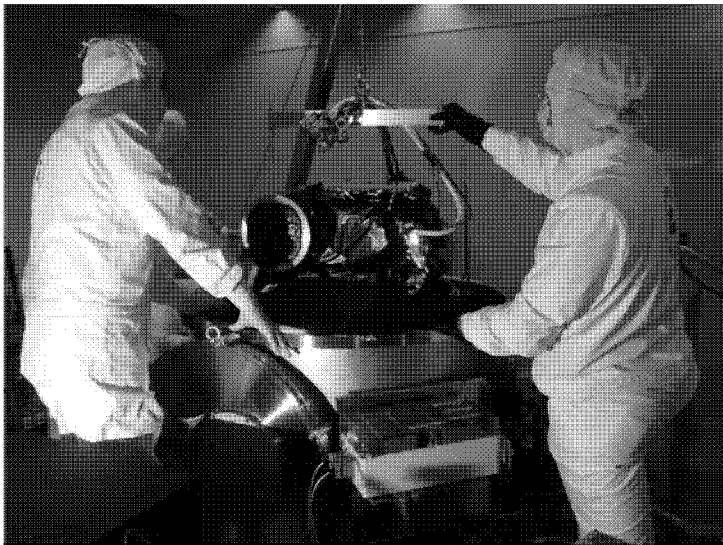
Figure 36. OSIRIS in ground calibration.

dependence), geometric distortion, as well as electrical offset and system gain of the CCD readout chain were successfully tested. More than 300 Gbyte of data were acquired with the OSIRIS system at MPS.

17.2. IN-FLIGHT CALIBRATION CONCEPT

The OSIRIS instrument is required to operate over a period of 11 years in a harsh radiation environment. The geometric distortion of the cameras needs to be re-measured in flight because it might have changed during launch. The relative alignment of the cameras can be affected by the change from the 1 g ground environment to zero gravity in space. It is certain that the detectors will be affected by energetic particles during cruise leading to changes in the detector dark current and charge transfer efficiency. The optics might be sputtered by energetic particles, and the primary mirrors might eventually further deteriorate because of dust particle impacts. Pinholes might be created in the filters. Accurate calibration of the image data can therefore only be obtained if additional in-flight calibration is performed. The approach to in-flight calibration is summarised by Table IX.

Dark current images are potentially costly in terms of data volume, but must be acquired to reveal detector radiation damage. Ground-based distortion maps are adopted as a baseline for optical correction, but require verification by observation of star fields. This is fairly straightforward using, e.g., fields studied by Landolt (1992). The co-alignment of the cameras can be determined by observation of star

TABLE IX

In-flight calibration methods.

| Item	Method
Bias and dark current	Shutter closed, opaque filter combination
Dark current dependence on temperature	Shutter closed, varying instrument heater parameters
Geometric distortion	Observation of star fields
Co-alignment	Observation of specific stars
Flat-fielding	Door closed, calibration lamps on, comparison with ground-based data, or smeared exposure on extended sources
Scattered light	Observation at different solar elongations, observation of extended objects (Mars, Earth, Moon)
Linearity and shutter performance	Multiple exposures at different exposure times
Point spread function	Star observations
Relative spectral response	Solar analogue stars and solar system objects
Absolute calibration	Standard star observations

TABLE X

Photometric standards used for absolute response calibration.

| Right Ascen-sion (2000)	Declination (2000)	Name	HR	HD	V (mag)	Spectral type	Remarks
02 28 09.4	+08 27 36	73 Cet	718	15318	4.28	B9III	Hamuy *et al.*
04 50 36.8	+08 54 02	2 Ori	1544	30739	4.37	A1Vn	Hamuy *et al.*
08 10 49.3	+74 57 58	BD +75D325	–	–	9.55	O5p	HST
08 43 13.6	+03 23 55	Eta Hya	3454	74280	4.3	B3V	Hamuy *et al.*
10 48 23.5	+37 34 13	BD +38D2179	–	93521	6.99	O9Vp	HST
11 36 41.1	−09 48 08	Theta Crt	4468	100889	4.69	B9.5Vn	Hamuy *et al.*
13 09 57.1	−05 32 18	Theta Vir	4963	114330	4.38	A1IVs+Am	Hamuy *et al.*
14 45 30.4	+00 43 03	108 Vir	5501	129956	5.7	B9.5V	Hamuy *et al.*
18 36 56.3	+38 47 01	Vega	7001	172167	0.03	A0V	HST
19 54 44.7	+00 16 26	58 Aql	7596	188350	5.61	A0III	Hamuy *et al.*
20 47 40.4	−09 29 43	Eps Aqr	7950	198001	3.77	A1V	Hamuy *et al.*
21 51 11.1	+28 51 52	BD +28D4211	–	–	10.51	Op	HST
22 41 27.5	+10 49 53	42 Peg	8634	214923	3.4	B8V	Hamuy *et al.*
00 01 49.4	−03 01 39	29 Psc	9087	224926	5.1	B7III-IV	Hamuy *et al.*

fields and of specific stars. Those are the same photometric standards that provide point spread function (PSF) and spectral response calibration. A list of photometric standards for OSIRIS is given in Table X. Relevant data can be found in Hamuy *et al.* (1992, 1994), Bessell (1999), and the HST CalSpec data base (HST CalSpec, 2005).

The most complicated task is flat-fielding. To facilitate this, both cameras carry main and redundant calibration lamps that can be turned on to illuminate the front doors when they are closed. The disadvantage of this approach is that the illumination of the telescope aperture is not uniform, neither in the NAC nor in the WAC. Therefore, only changes in the flat field between ground testing and in-flight can be determined. A complicating factor is that the calibration lamps have a limited lifetime. Hence, the main lamps will be cross-calibrated against the redundant lamps on an occasional basis (with the redundant lamps otherwise left off) to compensate for deterioration over time. Attempts will also be made to check the flat-fields by taking long exposures of the cometary nucleus during spacecraft slews.

The first images taken with the OSIRIS cameras are shown in Figures 37 and 38. These are 'random' star fields (i.e. without requesting specific spacecraft pointing) that showed that the performance of OSIRIS lives up to expectations. A more detailed discussion of calibration issues is the topic of a dedicated paper.
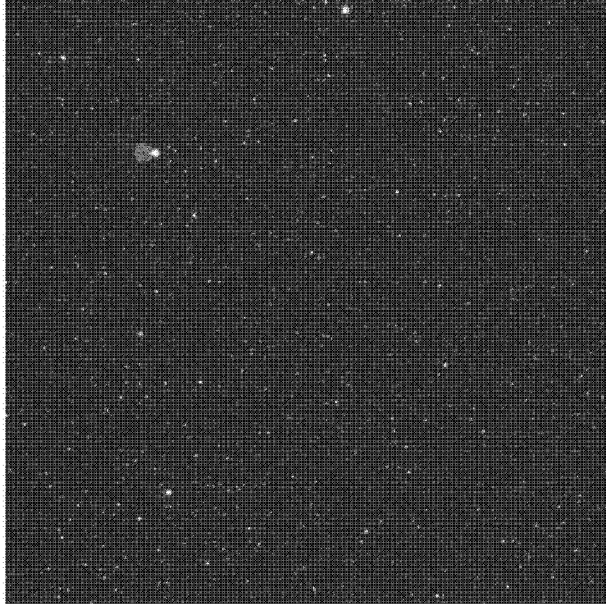
Figure 37. First light with the NAC, 5 s exposure with clear filter (FFP-VIS + FFP-IR).
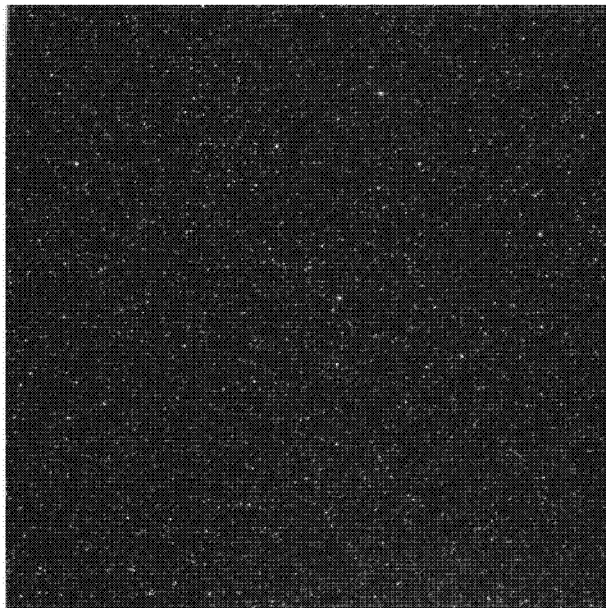
Figure 38. First light with the WAC, 5 s exposure with the red broad band filter. The WAC image contains the NAC view at the centre 1/5 FOV (horizontally mirrored).

18. Operations

OSIRIS is operated via the Rosetta spacecraft instrument timeline (ITL). The time-line allows commands to be executed at a specified time or relative to timeline events (for example: time of closest approach to Earth). ITL command sequences are transferred to the instrument using Orbiter Operational Requests.

OSIRIS supports the use of high-level UDPs (see Section 15). UDP commands can initiate a single image acquisition as well as complex observational scenarios. Hence, UDPs represent a toolbox that can be used for scientific observations. Approved UDPs have a higher reliability than dispatching a bulk of single commands from the mission timeline. It has been suggested therefore to implement substantial observation tasks, for example for the asteroid fly-bys, by single UDPs. Commanding via UDPs definitely will be the preferred way to operate the OSIRIS cameras.

It is envisioned that the science team will develop and implement UDPs for its specific scientific investigations. These new UDPs can be easily merged into the onboard software after validation on the ground reference model of OSIRIS.

19. Conclusions

There were considerable difficulties during the selection phase of the scientific imaging system of the Rosetta mission. However, the OSIRIS design concept that

Figure 39. Colour composite of the Orion nebula M42, obtained with the OSIRIS NAC during commissioning.

Figure 40. OSIRIS catching a glimpse of Earth and Moon from 73 million km distance.

was finally approved promised an instrument that would provide an outstanding scientific return. Many strict requirements were placed on the system during the design phase (e.g. operational lifetime, stray light, shutter accuracy, filter wheel speed, CCD readout rate). Most of these were achieved with only modest reduction of requirements in one or two areas where technical constraints demanded. The data to be returned by OSIRIS will provide a comprehensive survey of the nucleus of comet 67P/Churyumov-Gerasimenko and the surrounding dust and gas coma. OSIRIS will also make a major contribution to asteroid science through its multi-spectral capability. Its design is such that even in 2014 a superior system would be difficult to build.

Two examples of the quality of OSIRIS images are presented in Figure 39, the Orion nebula M42 obtained with the NAC in commissioning, and Figure 40, a glimpse back on Earth and Moon, acquired during the Rosetta pointing campaign from a distance of nearly 0.5 AU.

Acknowledgements

Sebastian, S. Stelzer, U. Strohmeyer, T. Tzscheetzsch, M. Wassermeyer (Germany), B. Johlander (ESTEC), M. Baessato, P. F. Brunello, S. Casotto, F. Don·, M. Lazzarin, E. Marchetti, F. Marzari, P. G. Nicolosi, F. Peron, F. Rampazzi, B. Saggin, G. Tondello, S. Verani, P. Zambolin† (Italy), J. Lagerros, and B. Davidsson (Sweden).

References

Abbey, A., Holland, A., Lumb, D., and McCarthy, K.: 1991, *Proceedings ESA Electronic Comp. Conference*, ESA SEE-N91, p. 307.

Adams, J. B.: 1974, *J. Geophys. Res.* **79**, 4829.

A'Hearn, M. F., Belton, M. J. S., Delamere, W. A., Kissel, J., Klaasen, K. P., McFadden, L. A., *et al.*: 2005, *Science* **310**, 258.

Bessell, M. S.: 1999, *Publ. Astron. Soc. Pacific* **111**, 1426.

Birk, M.: 1992, SUMER DPU Command Language (SCL), DPU-IF-E-0200-01-KT, Kayser-Threde GmbH, Munich.

Brunello, P., Peron, F., Barbieri, C., and Fornasier, S.: 2000, in Fischer, R. E., Johnson, R. B., Smith W. J., and Swatner W. H. (eds.), *Current Development in Lens Design and Optical Systems Engineering*, SPIE 4093, p. 79–88.

Calvel, B., Castel, D., Standarovski, E., Rousset, G., and Bougon, M.: 1999, **3785**, 56.

Campbell, D. B., Harmon, J. K., and Shapiro, I. I.: 1989, *Astrophys. J.* **338**, 1094.

Christen, A., Wiest, R., Rastetter, P., Weih, E., Fichna, T., Brüggemann, M., *et al.*: 2000, *Proceedings DASIA 2000*, ESA SP-457, p. 199–210.

Colwell, J. E.: 1997, *Icarus* **125**(2), 406.

Dale, C.: 1993, *IEEE Trans. Nucl. Sci.* **40**(6), 1628.

Debei, S., Fornasier, S., Ramous, P., Barbieri, C., Da Deppo, V., Brunello, P., *et al.*: 2001, *UV/EUV and Visible Space Instrumentation for Astronomy and Solar Physics*, SPIE 4498, p. 324–334.

Divine, N., Fechtig, H., Gombosi, T. I., Hanner, M. S., Keller, H. U., Larson, S. M., *et al.*: 1986, *Space Sci. Rev.* **43**, 1.

Dohlen, K., Saisse, M., Claeysen, G., Lamy, P., and Boit, J.-L.: 1996, *Opt. Eng.* **35**, 1150.

Donn, B.: 1991, in *Comets in the Post-Halley Era I*, Newburn, R. L., and Rahe, J. (eds.), Kluwer Academic Publishers, p. 335–359.

Fichna, T., Gärtner, F., Gliem, F., and Rombeck, F.: 1998, *Proceedings FTCS-28*, Munich, p. 408–413.

Gutiérrez, P. J., Ortiz, J. L, Rodrigo, R., and López-Moreno, J. J.: 2000, *Astron. Astrophys.* **355**, 809.

Gutiérrez, P. J., Jorda, L., Samarasinha, N. H., and Lamy, P.: 2005, *Planet Space Sci.* **53**, 1135.

Hamuy, M., Walker, A. R., Suntzeff, B., Gigoux, P., Heathcote, S. R., and Phillips, M. M.: 1992, *PASP*, **104**, 533.

Hamuy, M., Walker, A. R., Suntzeff, N. B., Gigoux, P., Heathcote, S. R., and Phillips, M. M.: 1994, *PASP*, **106**, 566.

Hapke, B.: 1993, *Theory of Reflectance and Emittance Spectroscopy*, Cambridge University Press, Cambridge, New York, Melbourne.

Holland, A., Abbey, D., Lumb, D., and McCarthy, K.: 1990, *SPIE* **1344**, 378.

Hopkinson, G. R.: 1989, *IEEE Trans. Nucl. Sci.* **36**(6), 1865.

HST CalSpec: 2005, Web page http://www.stsci.edu/hst/observatory/cdbs/calspec.html.

Huebner, W. F., Boice, D. C., Reitsema, H. J., Delamere, W. A., and Whipple, F. L.: 1988, *Icarus* **76**, 78.

Keller, H. U., Kramm, R., and Thomas, N.: 1988, *Nature* **331**, 227.

Keller, H. U.: 1989, *ESA Physics and Mechanics of Cometary Materials*, p. 39–45.

Keller, H. U., Knollenberg, J., and Markiewicz, W. J.: 1994, *Planet. Space Sci.* **42**(5), 367.

Keller, H. U., Curdt, W., Kramm, J. R., and Thomas, N.: 1995, in Reinhard, R., and Battrick, B. (eds.), *Images of the nucleus of comet Halley*, ESA SP-1127.

Keller, H. U., Britt, D., Buratti, B. J., and Thomas, N., 2004, in M. C. Festou, H. U. Keller, and H. A. Waever (eds.), *Comets II*, University of Arizona Press, Tucson, p. 211–222.

Keller, H. U., Jorda, L., Küppers, M., Gutiérrez, P. J., Hviid, S. F., Knollenberg, J., *et al.*: 2005, *Science* **310**, 281.

Kramm, J. R., and Keller, H. U.: 2000, in *Optical Detectors for Astronomy II*, Amico, P., and Beletic, J. W. (eds.), Kluwer Academic Publishers, p. 55–62.

Kramm, J. R, Sierks, H., Barthol, P., Müller, R., Tomasch, G., and Germerott, D.: 2003, Benefit from annealing proton irradiation defects on the OSIRIS CCDs, MPAE Report MPAE-W-472-03-02, Max-Planck-Institut für Aeronomie, Katlenburg-Lindau, Germany.

Kramm, J. R., Keller, H. U., Müller, R., Germerott, D., and Tomasch, G.: 2004, in *Scientific Detectors for Astronomy – The Beginning of a New Era*, Amico, P., Beletic, J. W., and Beletic, J. E. (eds.), Kluwer Academic Publishers, p. 131–135.

Kührt, E. and Keller, H. U.: 1994, *Icarus* **109**, 121.

Kührt, E.: 2002, *Earth, Moon and Planets* **90**(1), 61.

Küppers, M., Bertini, I., Fornasier, S., Gutiérrez, P. J., Hviid, S. F., Jorda, L., *et al.*: 2005, *Nature* **437**, 987.

Landolt, A. U.: 1992, *Astron. J.* **104**, 340.

McDonnell, J. A. M., Lamy, P. L., and Pankiewicz, G. S.: 1991, in Newburn, R. L., Neugebauer, M., and Rahe, J. H. (eds.), *Comets in the Post-Halley Era*, Kluwer Academic Publishers, p. 1043–1073.

Naletto, G., Da Deppo, V., Pelizzo, M. G., Ragazzoni, R., and Marchetti, E.: 2002, *Appl. Opt.* **41**(7), 1446.

Naletto, G., Boscolo, A., Wyss, J., and Quaranta, A.: 2003, *Appl. Opt.* **42**(19), 3970.

Possnert, G., Lagerros, J., and Rickman, H.: 1999, in *Advances in Optical Interference Coatings*, SPIE 3738, p. 428–435.

Richter, K., and Keller, H. U.: 1995, *Icarus* **114**, 355.

Rodionov, A. V., Jorda, L., Jones, G. H., Crifo, J. F., Colas, F., and Lecacheux, J.: 1998, *Icarus* **136**, 232–267.

Sagdeez, R. Z., Smith, B., Szego, K., Larson, S., Toth, I., Merenyi, E., *et al.*: 1987, *Astron. Astrophys.* **187**, 835.

Schleicher, D. G., Millis, R. L., and Birch, P. V.: 1998, *Icarus* **132**(2), 397.

Simonelli, D. P., Thomas, P. C., Carcich, B. T., and Veverka, J.: 1993, *Icarus* **103**, 49.

Smith, B., Szego, K., Larson, S., Merenyi, E., Toth, I., Sagdeev, R. Z., *et al.*: 1986, in *Proceedings of the 20th ESLAB Symposium on the Exploration of Halley's Comet*, Battrick, B., Rolfe, E. J., and Richard, R. (eds.), ESA SP-250, p. 327–331.

Thomas, N., and Keller, H. U.: 1987, *Astron. Astrophys.* **187**, 843.

Thomas, N., Boice, D. C., Huebner, W. F., and Keller, H. U.: 1988, *Nature* **332**, 51.

Thomas, P. C., Veverka, J., Simonelli, D., Helfenstein, P., Carcich, B., Belton, M. J. S., *et al.*: 1994, *Icarus* **107**, 23.

Thomas, P. C., Black, G. J., and Nicholson, P. D.: 1995, *Icarus* **117**, 128.

Thomas, N., Keller, H. U., Arijs, E., Barbieri, C., Grande, M., Lamy, P., *et al.*: 1998, *Adv. Space Res.* **21**(11), 1505.

Tomasch, G., Harboe-Sørensen, R., Müller, R., and Tzscheetzsch, T.: 2000, in *IEEE Nuclear and Space Radiation Effects Conference*, IEEE 00TH8527, p. 26–31.

Tsou, P., Brownlee, D. E., Anderson, J. D., Bhaskaran, S., Cheuvront, A. R., Clark, B. C., *et al.*: 2004, *J. Geophys. Res.* **109**, E12S01.

Vilas, F.: 1994, *Icarus* **111**, 456.

Weissman, P. R.: 1986, *Nature* **320**, 242.